1993ApJ...412..550Q

THE ASTROPHYSICAL JOURNAL, 412:550–567, 1993 August 1

THE WARPED DISK OF CENTAURUS A IN THE NEAR-INFRARED

A. C. QUILLEN,[1] JAMES R. GRAHAM,[2,3] AND JAY A. FROGEL[4]

Received 1992 October 20; accepted 1993 January 27

ABSTRACT

We present infrared images of Cen A (NGC 5128) in the *J*, *H*, and *K* bands. The infrared morphology is primarily determined by the presence of a thin absorptive warped disk. By integrating the light of the underlying prolate galaxy through such a disk, we construct models which we compare with infrared and X-ray data. The geometry of the warped disk needed to fit the IR data is consistent with a warped disk which has evolved as a result of differential precession in a prolate potential. The disk has an inclination, with respect to the principal axis of the underlying elliptical galaxy, that is higher at larger radii than in the inner region.

A scenario is proposed where a small gas-rich galaxy infalling under the force of dynamical friction is tidally stripped. Stripping occurs at different times during its infall. The orientation of the resulting gas disk depends upon the angular momentum of the infalling galaxy. We find that the resulting precession angle of the disk is well described by the precession model, but that the inclination angle may vary as a function of radius. We propose an orbit for the infalling galaxy that is consistent with the geometry of the warped disk needed to fit our infrared data, and rotation observed in the outer part of the galaxy.
same region.

Subject headings: galaxies: individual (NGC 5128) — galaxies: interactions — galaxies: ISM — galaxies: kinematics and dynamics — galaxies: structure — infrared: galaxies

1. INTRODUCTION

The nearest of all the giant radio galaxies,[5] Centaurus A (NGC 5128, Cen A), provides a unique opportunity to observe the dynamics and morphology of an active galaxy at a variety of different wavelengths. Because of the disk of gas and dust in its central region, Cen A is suspected to be the product of the merging of a small gas-rich spiral galaxy with a larger elliptical galaxy (Baade & Minkowski 1954). Shell-like features predicted in numerical simulations of galaxy collisions (Hernquist & Quinn 1988, 1989) have actually been observed in Cen A over a large range of distance from the nucleus (Malin, Quinn, & Graham 1983). Evidence of merging is correlated to activity in radio galaxies; for example, the two nearest radio galaxies (Cen A and Fornax A) have both shell-like stellar features and gas. Powerful radio galaxies appear to be in regions of higher galaxy density than less powerful ones (Heckman, Carty, & Bothun 1985). Many of them have complicated optical morphologies displaying features such as tidal tails, fans, shells, and dust features (Heckman et al. 1986). By studying the kinematics and morphology of the dust lane of Cen A, we may hope to learn how a merger could have caused the overall appearance of Cen A.

The dust and gas in Cen A have been traced in a variety of different wavelengths and species over a large range of radii from the nucleus, including H I (van Gorkon et al. 1990), Hα (Bland, Taylor, & Atherton 1987), CO(2–1) (Phillips et al. 1987; Quillen et al. 1992 hereafter QZPP), near-infrared (Giles et al. 1986; Joy et al. 1991; Turner et al. 1992), far-infrared (Eckart et al. 1990; Marston & Dickens 1988; Joy et al. 1988), in absorption against the optical light of the inner region (Dufour et al. 1979), and out to 10 kpc from the nucleus (Malin, Quinn, & Graham 1983). Here we present large-scale infrared mosaics in the *J* (1.2 μm), *H* (1.6 μm), and *K* (2.2 μm) bands of the inner region containing the dust lane.

The optical morphology of the dust lane has been modeled as a transient by Tubbs (1980), and as an equilibrium structure in a rotating triaxial galaxy by van Albada, Kotanyi, & Schwarzschild (1982). The observed stellar rotation does not support the latter interpretation (Wilkinson et al. 1986). QZPP found that the kinematics of the CO gas in the inner region ($r < 70''$) (where *r* is the distance from the nucleus of the galaxy) was not consistent with noncircular motion on a principal plane of a triaxial galaxy. However, Nicholson, Bland-Hawthorne, & Taylor (1992) and QZPP find that the kinematics of both the ionized and molecular gas is well modeled by a warped disk composed of connected rings undergoing circular motion. In Tubbs' (1980) model, the gas disk is assumed to be initially on a plane that is not a principal plane of the underlying galaxy. The gas disk then evolves into a warped shape as a result of differential precession. This type of model was successfully used to fit the CO data of Cen A in the inner region ($r < 70''$)(QZPP) and has reproduced the morphology of other galaxies, most notably the remarkably twisted disk of NGC 4753 (Steiman-Cameron, Kormendy, & Durisen 1992).

Nicholson et al.'s (1992) model for the warped disk has an outer fold which is consistent with the optical appearance of the dust lane and an inner fold (at $\sim 30''$) which corresponds to a fold at the same radius in the model of QZPP, but differs from QZPP by having the northern side of this fold toward us instead of away from us. Because the disk is both geometrically thin and optically thin in both CO (QZPP) and Hα (Bland et al. 1987), the velocities fields from the CO and Hα are symmetrical about the origin, and it is difficult to determine which side of the disk is toward us. However, in the near-infrared, it is possible to see through the outer fold (prominent optically)

---

[1] Theoretical Astrophysics, 130-33, California Institute of Technology, Pasadena, CA 91125.

[2] Astronomy Department, University of California, Berkeley, CA 94720.

[3] Alfred P. Sloan Research Fellow.

[4] Ohio State University, Astronomy, 174 West 18th Avenue, Columbus, OH 43210.

[5] We use a distance of 3 Mpc to Cen A (Tonry & Schechter 1990).

into the inner region ($r < 70''$). Since the morphology in the near-infrared is determined primarily by the absorptive proprties of the disk, the morphology is not symmetrical about the nucleus. It is possible to compare to the models derived from kinematic data and resolve their differences. Our near-infrared data extends previous images of the nucleus of Cen A in the near-infrared (Giles 1986; Joy et al. 1991; Turner et al. 1992) and has a field of view large enough to cover both the optical dust lane and the region observed in CO and Hα.

Since the morphology of the infrared data is determined primarily by the warped disk, we devote the first half of our paper to verifying the geometry of the warp, and to determining the opacity of the warped disk. In order to do this, we integrate the light of the galaxy using a purely absorptive model for the warped dusty disk (described in § 3) and compare the results of the integration with our data (§ 4). Our model for the geometry of the gas disk is based upon the model used to fit the CO data (QZPP). A modification of this model, in which the gas disk is at a higher inclination (with respect to the axis of symmetry of the potential) at large radii ($r > 80''$) than in the inner region fits the infrared morphology and colors remarkably well.

Much of the interpretation of observations in the nuclear region of Cen A relies on accurate knowledge of the location and opacity of the gas disk. In § 4 we discuss the differences between the data and our model and predictions for X-ray absorption. We find that observation of a one-sided X-ray jet cannot be acounted for by absorption of X-rays on the other side of the nucleus by the gas disk. Since our models do not have an elongation of the *J* and *H* isophotes at the nucleus which is seen in our data, we support Joy et al.'s (1991) interpretation of this elongation as evidence for an infrared jet. We interpret extended features observed in the *K* isophotes 30″–50″ from the nucleus that are not predicted in our purely absorptive model for the disk, as emission in K from the disk. In § 4.1 possible emission sources are discussed.

In § 5, we propose a scenario for the merger, based on the infall by dynamical friction of a spiral galaxy into a large elliptical. We find an orbit for the infalling spiral that is consistent with our model for the data constructed in § 3. A discussion follows in § 6.

2. OBSERVATIONS

We obtained near-infrared images of Cen A with the IR imager at CTIO on 1989 May 7–9 with the 1.5 m telescope. Each pixel of the imager projects to 0″.89 on the sky and the resultant field of view is 51″.6 × 55″.2. Images were obtained in the standard *J* (1.24 μm), *H* (1.65 μm), and *K* (2.16 μm) photometric bands.

Most of the data presented here were obtained on May 7 and 9. The photometric stability was determined from photometry of the Elias et al. (1982) standards GL 390, HD 161743, and HD 106965, which demonstrated that the photometric zero point was stable to better than 0.15 mag. This level of photometric accuracy is sufficient for the current study of Cen A, which is primarily morphological. The seeing was typically 1″.7 (full width half-maximum after a 60 s integration in *J* and *H*). The observations were combined into mosaics, presented in Figures 1, 2, and 3 after correction for the slight nonlinearity of the array, sky subtraction, flat-fielding, and correction for residual sky background variations. In Figures 1–3 the maximum and minimum surface brightness levels where chosen in order to show the dust features at high contrast. (See Figs. 7*a*–9*a* below [contour plots] for detail at the nucleus.)

Data were obtained in pairs of object-sky fields. Each frame in *H* and *J* consists of three 60 s exposures and in *K* consists of six 30 s exposures. The position for the sky frames was $\simeq 30'$ either to the east or west from the nucleus of the galaxy so that

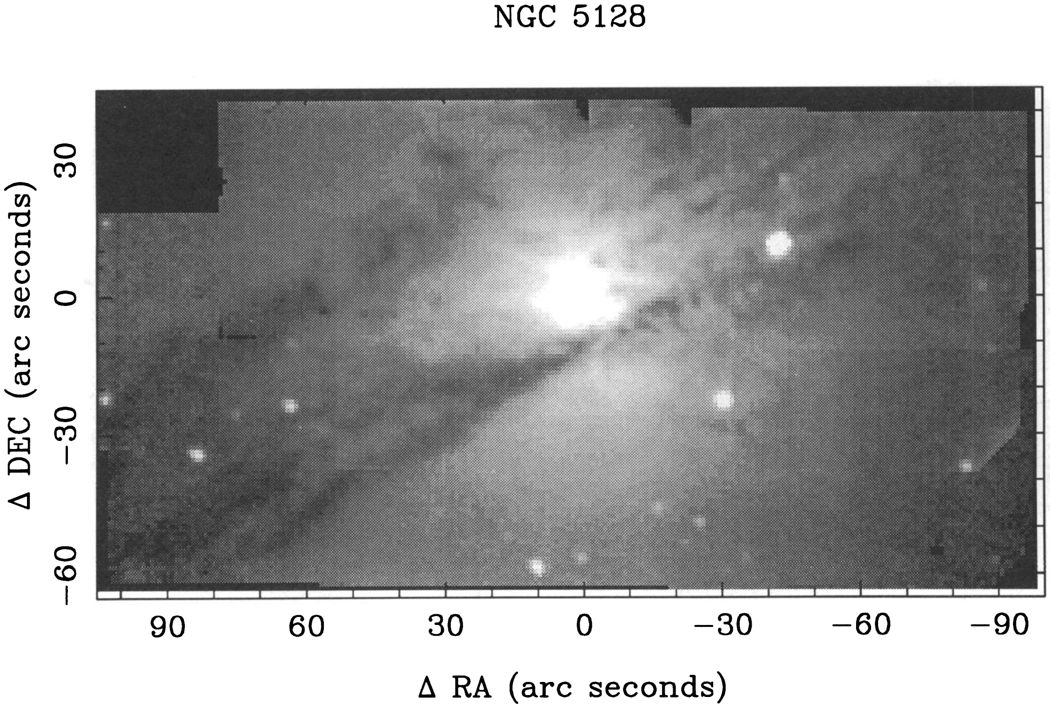

FIG. 1.—*J* (1.24 μm) mosaic of NGC 5128 in magnitudes per square arcsecond. The range shown is 15.0–18.0 mag per square arcsecond. See Fig. 7*a* for detail at the nucleus.

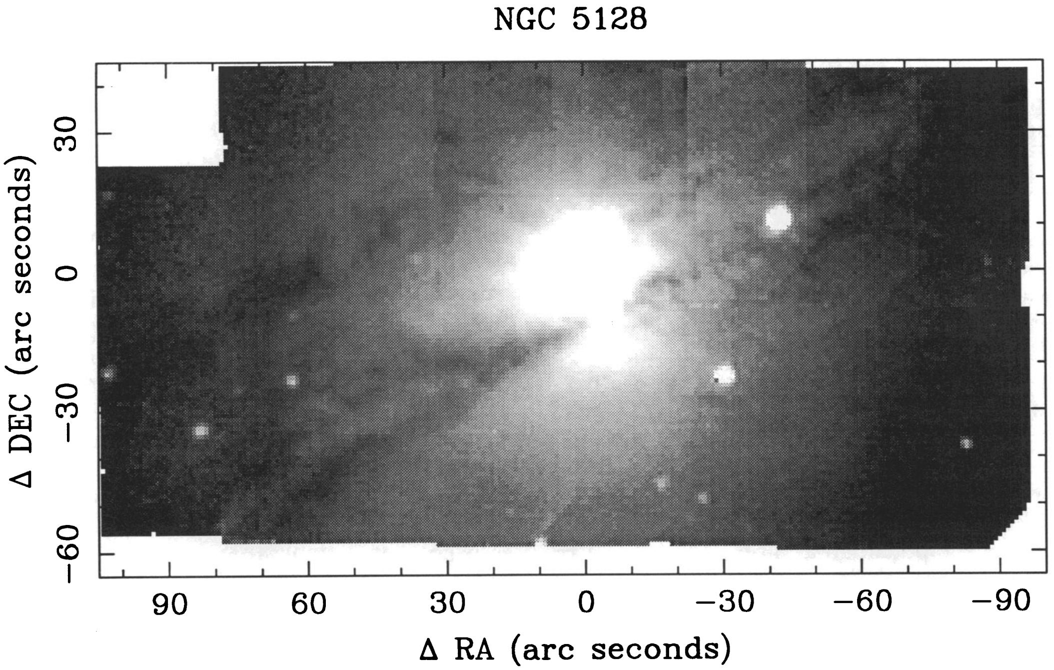

FIG. 2.—*H* (1.65 μm) mosaic of NGC 5128 in magnitudes per square arcsecond. The range shown is 14.8–17.0 mag per square arcsecond. See Fig. 8*a* for detail at the nucleus.

the sky frames are uncontaminated by galaxian light. The first stage of reduction was to perform pair-wise subtraction of the adjacent sky frames. Gain variations across the detector array were then corrected by dividing by dome flats. As a consistency check, we compared the dome flats with a flat made from a dark subtracted average sky and found no significant difference.

The area observed was covered using a rectangular R.A.-Decl. grid of three rows. Each row was observed with an offset in R.A. of $\simeq 25''$, or approximately half the field of view. The declination offset between the rows was also $\simeq 25''$. Therefore the central $\simeq 50''$ is covered 4 times, and most of the edges twice. A total of 20 frames in each band were obtained. Telescope offsets were unreliable and therefore the relative positions of the fields comprising the mosaic were determined from the position of stars in the individual frames. The resultant

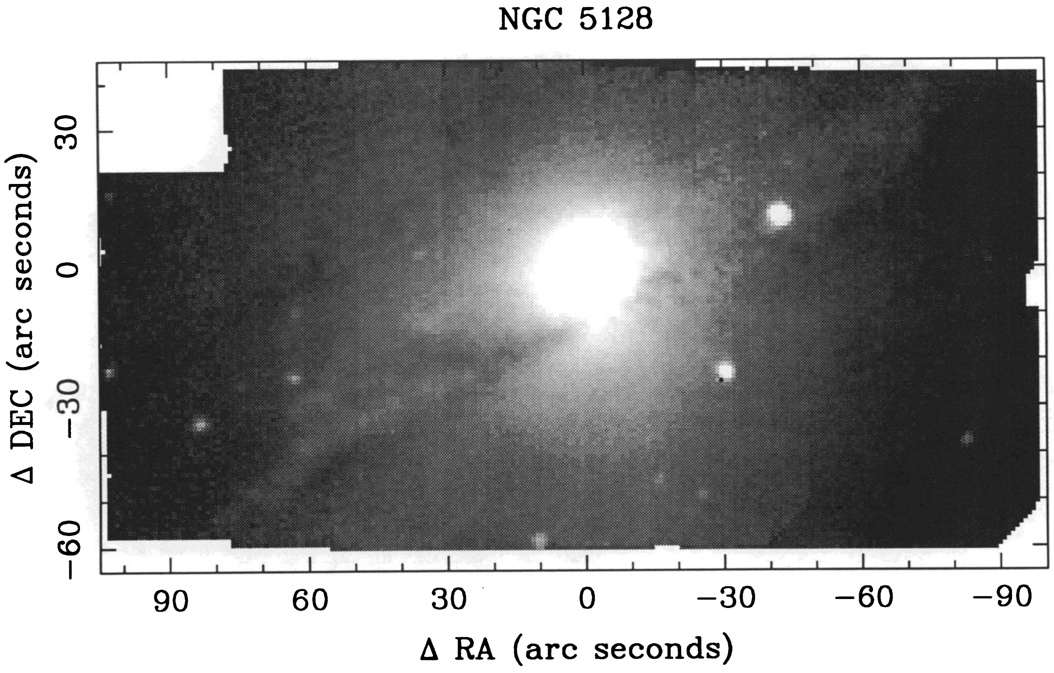

FIG. 3.—*K* (2.16 μm) mosaic of NGC 5128 in magnitudes per square arcsecond. The range shown is 14.0–16.5 mag per square arcsecond. See Fig. 9*a* for detail at the nucleus.

registration is good to 1″ over the entire mosaic. Registration offsets degraded the resolution of the mosaics to 2″–3″ (full width half-maximum of a point source).

Despite our efforts to ensure accurate sky subtraction by obtaining sky measurement immediately after the object frames, residual sky variations are present in the reduced frames. Therefore, in constructing the final mosaic we adjusted the background level in each frame until the difference between overlap regions was zero. This process was successful, and frame boundaries are difficult to see in Figures 1, 2, and 3. The sum of the frame offsets is constrained to be zero so that no spurious sky offset is introduced, and the sky level in the final mosaic is as close to zero as permitted by sky level variation during the observations. The resultant sky level uncertainty corresponds to 16.6 mag per square arcsecond at *K*, 16.5 mag per square arcsecond at *H*, and 18.1 mag per square arcsecond at *J*.

Some additional data were obtained on May 8. This night was mostly cloudy, except for a brief clear spell during which the three frames which complete the NW corner of each mosaic were obtained. These data are clearly inferior to the data obtained on the May 7 and 9 due to large transparency variations. They are included in the mosaic for completeness after making a crude compensation for transmission based on standard stars. Inspection of the mosaic shows that this is apparently successful because these frames blend seamlessly with the rest of the mosaic. However, we place low significance on the morphology and colors in this part of the mosaic, and no conclusions are based on that part of the image.

In order to improve our photometric accuracy, calibration was done by matching to the aperture photometry of Turner et al. (1992) at the position of the 2.2 μm nucleus. Their photometric accuracy was uncertain by 0.18 mag in *J* and *H* and by 0.13 magnitudes in *K*.

The morphology of our data is primarily determined by the presence of an absorptive thin dusty warped gas disk. Such a disk at high inclination with respect to the line of sight presents higher optical depth at folds where the disk becomes tangent to the line of sight. Since the gas disk of Cen A is at high inclination we expect the prominent features of the infrared mosaics to correspond to folds in the gas disk. In Figure 1, lines of sight of higher optical depth are apparent both above and below the nucleus. The fainter fold seen primarily on the northeast side corresponds to a fold described by Nicholson et al. (1992) which from their Hα velocity field, they found to be at a radius from the nucleus of ~100″. This outer fold is prominent in optical pictures of Cen A and forms the northern boundary of the dust lane. On the southern side of the nucleus, there is a more prominent fold (which we expect is closer to the nucleus) which has been seen in the near-infrared previously by Giles et al. (1986) and Joy et al. (1991). Nicholson et al. (1992)'s model for the warped disk, depicted this inner fold so that the southern side was away from us instead of toward us as we observe it. Because of the symmetry of the Hα velocity field, it is not possible to determine from these data which side of the disk is closer to us. We suspect that the intensity of the Hα emission on the southern side is dimmer because there is more absorption from dust in the inner region ($r < 100''$) on the southern side of the disk. We note that the orientation of this inner fold is consistent with the model for the warp derived from the CO data, which was consistent with the shape of the southern side of the dust lane as seen in the optical. We expect this model to fit our infrared data well in the inner region where a good fit was found to the CO data ($r < 70''$). However, this model does not have an outer fold that corresponds to the northern fold observed in the infrared (at $r \approx 100''$) which forms the northern side of the dust lane. Therefore in order to fit the infrared data, the model must be modified for $r > 70''$ to include an outer fold.

Also observed in our data is an elongation to the NE (on a scale of 3″–10″) of the isophotes at the position of the nucleus in *J*, and *H*, that is aligned with the direction of the soft X-ray jet (Feigelson et al. 1981). This elongation has been interpreted as evidence for a one-sided infrared jet by Joy et al. (1991). In § 4.2, by comparing with the results of our models we attempt to determine whether this feature is an artifact of absorption through a warped dusty disk.

In *K*, extensions of the isophotes are observed to the SE and NW 30″–50″ from the nucleus that are not observable in the *J* and *H* mosaics. It is possible that these features are due to some emission from the disk. In § 4.1, possible emission sources are discussed.

The opacity of the dust is much less in *K* than in *J* and *H*. Primarily what is observed (except for at the location of the nucleus and the features discussed previously) is the old stellar population of the background elliptical galaxy. In the next section we use the surface brightness in *K* to determine the light distribution which we use to integrate the light of the galaxy through an absorptive warped disk. The resulting models can then be compared to our mosaics.

3. INTEGRATION OF LIGHT

In this section we discuss how the light from the underlying galaxy is integrated to simulate the infrared observations. Our simpe model integrates starlight along the line of sight in steps of 45 pc which corresponds to 3″ square pixels on the sky, given a density as a function of radius for the light of the background galaxy. The density function used is discussed in § 3.1. When integrating along the line of sight, every time the dusty disk is encountered, we multiply by a transmission coefficient. In § 3.2 we discuss the absorptive properties of the dusty disk which determine the transmission coefficients in *J*, *H*, and *K*. In § 3.3 we describe our model for the geometry of the warped gas disk.

3.1. *Background Galaxy*

In the *K* band the opacity of the dust is much less than in *J* or *H* and therefore gives the best measurement of the old stellar population of the background elliptical galaxy (except perhaps at the position of the nucleus ($r < 5''$) where the extinction is high, and there may be emission from an active nucleus). We use the surface brightness in *K* to determine the light distribution of the background galaxy. In Figure 4, surface brightness at *K* in magnitudes per square arcsecond is plotted against $r^{1/4}$ for an average of pixels in a narrow wedge of our data 10° wide extending from the nucleus to the eastern edge of the mosaic. We chose this region of the data because it was least contaminated by the dustlane. Pixels in the dust lane at the same radius are at most 0.6 mag per square arcsecond fainter than the points shown in Figure 4. The size of the error bars is determined by the uncertainty in the underlying sky level of the mosaic and the root mean square variation of the pixels used in the average. A variation of the base underlying sky level would cause a change in curvature primarily at large radii ($r > 40''$) on this plot.

1993ApJ...412..550Q

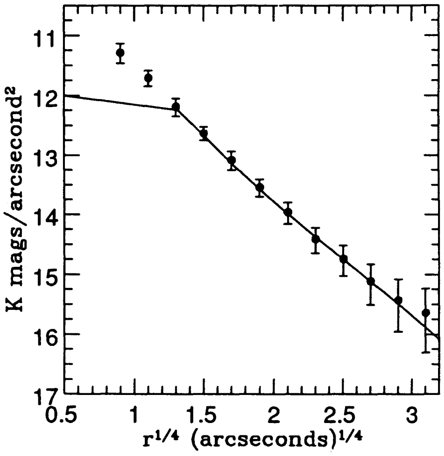

FIG. 4.—Surface brightness at K in magnitudes per square arcsecond vs. $r^{1/4}$. The points are at the average surface brightness of a wedge of the K mosaic that is 10° wide extending from the nucleus to the eastern edge of the mosaic. The error bar widths are determined from the scatter of the pixels used in the average, and the uncertainty in the underlying sky level. The solid line is the surface brightness from an integration of the light density we used to model our data (see Table 1 for the parameters of the model). The model at $r < 3''$ ($r^{1/4} < 1.3$) gives a poor fit to the data because the resolution of the model is 3″.

We need a simple analytic form for the density of the galaxy light. Figure 4 shows that the data at K obey a de Vaucouleurs ($r^{1/4}$) law (previously noted by Giles 1986) but with a smaller effective radius than is observed optically in the outer regions ($r > 80''$) of the galaxy (Dufour et al. 1979). This suggests that we use a Hernquist model (Hernquist 1990), which has a density distribution $\rho(r)$ described by

$$\rho(r) = \frac{M}{2\pi} \frac{r_0}{r(r + r_0)^3}, \qquad (3.1)$$

where r_0 is the effective scale length, and M is the mass of the galaxy. The scale length r_0 is related to the effective radius r_e of the de Vaucouleurs law by $r_0 = 1.8r_e$. However, the Hernquist model is only a good approximation to a de Vaucouleurs law over the range $0.1 < r/r_e < 16$, and we have data at $r/r_e < 0.1$. Therefore we model the background galaxy as the sum of two Hernquist models. We parameterize the sum of the two models with effective scale lengths r_0 and r_1 and the ratio μ of the two masses of the Hernquist models comprising the sum. We determined the larger scale length to be $r_0 = 168''$ from the effective radius observed optically in the outer part of the galaxy (Dufour et al. 1979). By varying r_1 and the ratio μ we found a good fit to the data assuming that the galaxy has constant mass to light ratio over the scale of our data, with $r_1 = 15''$ and $\mu = 0.05$. The resulting model is displayed as the solid line in Figure 4. The values we found for r_1 and μ are not significant because of the uncertainty in surface brightness of our data, but we give their values in order to describe the function we used for the density distribution.

The solid line in Figure 4 shows the integrated surface brightness of the density function chosen to model the background galaxy. This density function fits the data well. Since the surface brightness in the outer part of the mosaic is uncertain (due to a possible sky offset), the surface brightness of our model in the outer region is also uncertain. However, information inferred from morphological changes caused by absorption from the dusty warped disk, should be unaffected by the uncertainty in the absolute magnitude of the model in this region. By choosing this function for the light density of the galaxy, our model is consistent with both the effective radius observed from the de Vaucouleurs law optically in the outer region of the galaxy and the de Vaucouleurs law observed from infrared observations in the inner region. In addition, the rotation curve of Cen A as observed in H I is consistent with this model for the density (van Gorkom et al. 1990) assuming the approximately constant mass to light ratio observed by van Gorkom et al. (1990). We note that the rotation curve for this potential does not differ significantly over the range of radii of our data from the rotation curve we chose to describe the warp (see next section).

In order to integrate the light in J and H we assumed that the background galaxy had no color gradient and had colors $J-K = 1.2$ mag and $H-K = 0.30$ mag, which match the colors observed at the top left hand corner of the mosaics (see Figs. 10*a*–12*a* below) where there is little dust reddening. Within the photometric accuracy of our mosaics, these colors are the same as typical old stellar population colors (Frogel et al. 1978).

3.2. *Disk Absorption*

In Figure 5 we show a $J-H$, $H-K$ color-color plot for all the pixels in the J, H, and K mosaics. The offset from the color of a typical old stellar population is probably due to zero-point errors in our photometry. Since pixels mostly lie close to the reddening line (displayed as a solid line in Fig. 5), we use a purely absorptive model for the gas disk. We assume that there is no extinction anywhere but in the gas disk, and that the disk is thin (see discussion in QZPP for estimates of the thickness of the molecular disk). Our model ignores scattering by the dust.

Every time a fold of the warp is encountered the integrated intensity is multiplied by a transmission coefficient T, where $T = e^{-\tau}$ and τ is the opacity of the disk. The extinction $A(\lambda)$

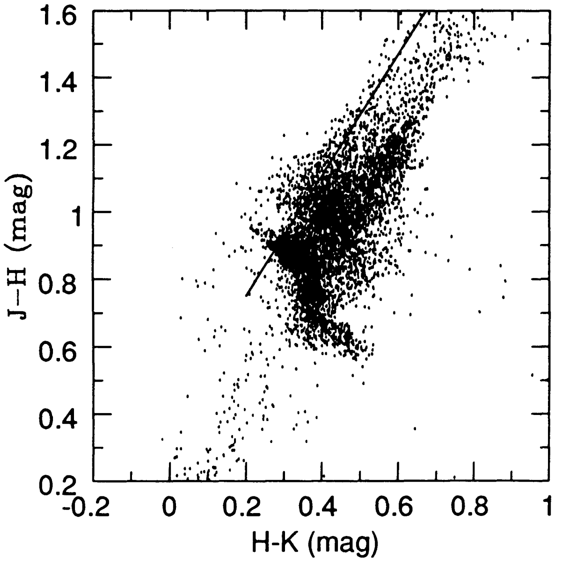

FIG. 5.—Color-color map $J-H$ vs. $H-K$ for the pixels in the three mosaics, excluding the right-hand side of the mosaic (those pixels with R.A. offset greater than 30″ from the position of the nucleus). The side of the mosaic was excluded because of the inferior quality of the data on this side of the mosaic (see § 2). The solid line is at the slope of the reddening line and begins at the position of the color of an old stellar population (Frogel et al. 1978). Offsets from this line are not significant since they are within the photometric accuracy of our mosaic.

at wavelength λ is given by $A(\lambda) \approx 1.08\tau(\lambda)$. We note that if the gas is patchy and can be described as having an area filling factor f_a, the transmission coefficient would $T = 1 - f_a(1 - e^{-\tau})$. For small values of f_a and τ the transmission can be approximated as $T \approx e^{-f_a\tau}$ so that $A(\lambda) \approx f_a\tau(\lambda)$ and $A(\lambda_1)/A(\lambda_2) = \tau(\lambda_1)/\tau(\lambda_2)$ for different wavelengths λ_1 and λ_2, which is independent of the filling factor. Since the molecular material in the disk has low area filling factor ($f_a < 0.1$, QZPP), and pixels in our data have colors primarily close to the typical Galactic reddening line (see Fig. 5), we suspect that this is a reasonable approximation. We note that if individual dust clouds absorbing light are optically thick, this approximation would not be valid. The extinction, $A(J)$, was varied for best fit to the morphology of the J mosaic, and the typical galactic extinction ratios from Mathis (1990) $A(K)/A(J) = 0.38$ and $A(H)/A(J) = 0.62$ were used to determine the absorption coefficients for H and K.

Since the disk is optically thin (in CO and Hα) except possibly at the folds (Bland et al. 1987 and QZPP), it is necessary to consider the opacity of the disk (or transmission coefficient in our integration) as a function of the local slope of the disk with respect to the line of sight. We can measure the local slope of the disk by computing a Jacobian, given by $J = \partial(x, y)_{\rm disk}/\partial(x, y)_{\rm sky}$ where $(x, y)_{\rm disk}$ is a local coordinate system on the gas disk, and $(x, y)_{\rm sky}$ is a Cartesian coordinate system on the sky. The Jacobian is the ratio of the projected area of a small piece on the disk to its real area. For $J < 2$, when the disk is close to face-on, in our integration we use a transmission coefficient $T = e^{-\tau}$ where $\tau = J\tau_p$, and τ_p is the opacity of the disk if it were viewed face-on. For $J > 2$, when the disk is at high inclination with respect to the line of sight, we use transmission coefficient derived from $\tau = h\tau_p$, for the opacity of a grid resolution element. This represents the opacity per unit length of a thick slab viewed edge-on.

We chose a simple function for the dust distribution as a function of radius r from the nucleus that decays exponentially at large radii, yet is not sharply peaked in the center. In our models the face-on absorption of the disk at J as a function of radius is given by

$$\tau_p(r) = \frac{B_J}{\exp\,[(r - b)/\sigma_\tau] + 1} \tag{3.2}$$

with constants B_J, b, and σ_r. B_J is the optical depth of the disk at J at the nucleus if the disk were observed face-on, b is the radius at which the opacity of the disk begins to decay, and σ_τ is its exponential decay rate.

3.3. *Tilted Ring Model, Precession from a Plane*

Our model for the geometry of the warped disk is based upon a model (QZPP) for the gas that gives the best fit to the ^{12}CO (2–1) data. This model, which fits the CO data well for $r < 70''$, is derived assuming that the gas has evolved from a planar system as a result of differential precession in a prolate potential (Tubbs 1980). It assumes that the inclination of the gas rings with respect to the principal axes of the potential is a constant as a function of radius and time.

We describe the orientation of the potential with the two angles ϑ and χ, where χ is the position angle on the sky of the projected axis of symmetry (z-axis) of the prolate potential, measured from north and ϑ is the angle between the line of sight and the z-axis (i.e., the inclination of the galaxy). We describe the geometry of the warp with two additional angles which are functions of r, the distance from the nucleus. We can think of a warp as a set of smoothly connected inclined rings each centered on the nucleus of the galaxy (e.g., Sparke 1986). We denote z' as the rotational axis of symmetry of a ring at radius r, and let $\omega(r)$ be the angle between the z- and z'-axes. We define $\alpha(r)$ to be the angle in the equatorial plane of the galaxy of the projection of z' onto this plane minus the angle of the projection of the line of sight (see Fig. 6 for a pictorial representation of these angles). In an axisymmetric potential of ellipticity ϵ_p, the precession rate $d\alpha/dt$ is approximately

$$\frac{d\alpha}{dt} \sim \frac{\epsilon_p v_c}{r}\,, \tag{3.3}$$

where v_c is the circular velocity at radius r. The ellipticity ϵ_p, is given by $\epsilon_p = 1 - 1/q$ where q is the axis ratio of the potential which for the nearly spherical systems that we are interested in, can be written approximately as a function of $x^2 + y^2 + z^2/q^2$. Prolate systems have $q > 1$ while oblate systems have $q < 1$. After a time Δt,

$$\alpha(r) = \epsilon_p \Omega \Delta t + \alpha_0\,, \tag{3.4}$$

where $\Omega = v_c/r$. We used the following rotation curve for the circular velocity v_c

$$v_c = \frac{Ar}{\sqrt{r^2 + c^2}}\,, \tag{3.5}$$

with constants A and c. For large radii ($r \gg a$), this rotation curve approaches a flat rotation curve, the rotation curve of an isothermal sphere with velocity dispersion $\sigma = v_c/(2)^{1/2}$. We note that the velocity curve of a galaxy with constant mass-to-light ratio and a surface density that follows a de Vaucouleurs $r^{1/4}$ law (as Cen A is observed to be; van Gorkom et al. 1990 and Dufour et al. 1979) is a reasonable approximation to the above rotation curve for non–large radii ($r \not\gg c$). We found a good fit to the CO data using a potential with a varying ellipticity $\epsilon_p = \epsilon_\infty[1 - \exp(-r^3/\sigma_{\rm el}^3)]$ where ϵ_∞ is the ellipticity far away from the nucleus, and $\sigma_{\rm el}$ gives the radius at which the

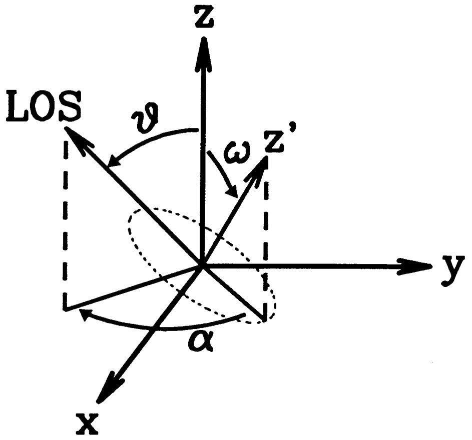

FIG. 6.—Definition of angles used to describe the warped disk. The x, y, and z axes are the principal axes of the potential. The z' axis is the axis of symmetry of the ring represented by the dotted ellipse. LOS is the line of sight. See § 3.3 for further details.

ellipticity begins to decay. We note that it is evident from the K mosaic, that Cen A becomes more spherical in the central regions, although because of the dust, it is difficult to accurately measure the ellipticity as a function of radius. (See Table 1 below for the parameters of the best fit to the CO data [QZPP]).

4. RESULTS OF MODELING

We found that the model from QZPP displays the morphology of the infrared data quite well in the central region ($r < 70''$) of the Galaxy. The best fit to the CO data found that the inclination of the principal axes of the potential with respect to the line of sight was $\vartheta = 65°$ and that the gas has an inclination of $\omega = 25 \pm 5°$ with respect to the principal axes of the potential. However, the geometry of the dust is different than that predicted by this model for $r > 70''$. In particular, the fold of gas observed on the northern side of the nucleus (see Fig. 1) that is also prominent optically and forms the northern side of the dust lane, is not seen in our model (see discussion in QZPP). From their Hα velocity field, Nicholson et al. (1992) found that the gas in this fold was at an inclination with respect to the line of sight of $i \approx 105°$. The gas in this outer fold is at inclination of at least $\omega = i - \vartheta \approx 40°$ degrees with respect to the principal axes of the potential. This inclination is significantly higher than that predicted by QZPP model for $r < 70''$. Because of this discrepancy, we find that the configuration of the gas in Cen A *is inconsistent with one of the assumptions of our previous model. Either the gas was not initially in a plane* [$\omega(r)$ *varies as a function of* r] or $\omega(r)$ evolved with time.

One mechanism that would account for large changes in the inclination of the gas rings with radius would be settling caused by viscosity between differentially rotating gas rings. However, the time scale $\Delta T \sim 10^8$ yr to create the warp by differential precession that we derived from fitting to the CO data with our previous model was less than the settling time scale derived by Steiman-Cameron & Durisen (1988; see QZPP for further details).

Another possibility is that the inclination of the gas resulted in some nontrivial way from the dynamics of the merger. If this were true, we would expect $\omega(r)$ to vary as a function of r. We found that we could reproduce the features of our infrared data by using a model with precession angle $\alpha(r)$ described by equation (3.4) but with inclination angle ω that increases from 20° to 40° at $r \approx 150''$. This new model is still consistent with the model derived from the CO data in the inner region ($r < 70''$) and has the outer fold at $\sim 100''$ that is observable in our infrared data. In § 5 we discuss a scenario for the merging of a small spiral galaxy with a larger elliptical. We propose that changes in the inclination of the gas disk can result from variations in the orbital angular momentum of the infalling spiral galaxy.

The results of integrating the light of the galaxy at a resolution of 3″ per pixel in the near-infrared for our new model are displayed in Figures 7–9 along with data at the same contour levels on the same scale. We chose this value for the resolution of the models in order to match the resolution of the mosaics. Color maps are shown in Figures 10–12. Parameters for constructing these models can be found in Table 1. The parameters for the geometry of the warp are mostly identical to those that gave the best fit to the CO data (from QZPP) (also shown in Table 1) except that the inclination angle, $\omega(r)$ is no longer a constant as a function of radius. The function for $\omega(r)$ is displayed as the dotted line in Figure 14*a* in § 5, below. There are slight differences in the orientation angles of the underlying galaxy, χ and ϑ, between our infrared model and the older CO model. Parameters for the light distribution of underlying galaxy (discussed in § 3.1) and absorptive properties of the disk (discussed in § 3.2) are also found in Table 1. Qualitatively our models agree very nicely with the data (see Figs. 7–12). The fold on the northern side of the dust lane that is at high inclination in our model is very similar to that observed in the data. Using the galactic extinction ratio to model the absorption of the disk in the different wavelengths seems to have reproduced the colors of the disk remarkably well.

The morphology of these models is primarily determined by the opacity of the disk at the folds. A good fit to the morphology of the data was found for $B_J = 0.15$. In our models the thickness of the disk $h < 3''$, which is not an unreasonably small value (see QZPP for limits on the thickness of the molecular disk.) Since the outer fold is more pronounced in the models than the data, it is likely that the disk is somewhat thicker than 3″ in the outer region ($r > 70''$). We note that the outer fold is visibly clumpy (see Figs. 1–3). Since our model assumed a smooth distribution for the gas, this may partly explain why this fold is more pronounced in the models. If the disk at large radii is not completely relaxed after the merger at larger radii (which could happen if the individual clouds composing the disk had low volume filling factor) we would expect the disk to be thicker in the outer regions. This would make the outer fold appear to be less sharp. The morphology of the inner fold seems to be well reproduced by the model, so that we doubt that the disk is thicker than 3″ in the inner region ($r < 70''$).

TABLE 1

MODEL PARAMETERS

A. Background Galaxy Parameters[a]

Parameter	Value
μ	0.05
r_0	168″
r_1	15″

B. Dust Parameters[b]

Parameter	Value
B_J	0.15
b	80″
σ_τ	80″

C. Warp Parameters[c]

PARAMETER	VALUE	
	Infrared[d]	CO[e]
ϑ	65°	60°
χ	30°	35°
A (km s^{-1})	300	300
c	40″	40″
σ_{el}	80″	80″
α_0	−182°	−182°
$\epsilon_\infty \Delta t$ (yr)	2×10^7	2×10^7
ω	...[f]	25° ± 5°

[a] See § 3.1 for description of parameters.

[b] See § 3.2.

[c] See § 3.3.

[d] Displayed in Figs. 7–13.

[e] From QZPP.

[f] See function shown in Fig. 14*a*.

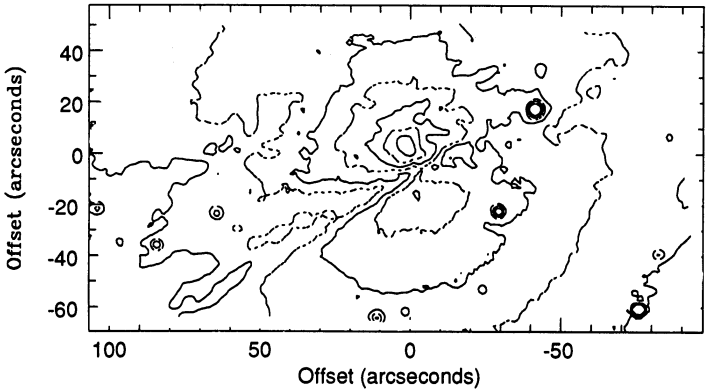

FIG. 7*a*

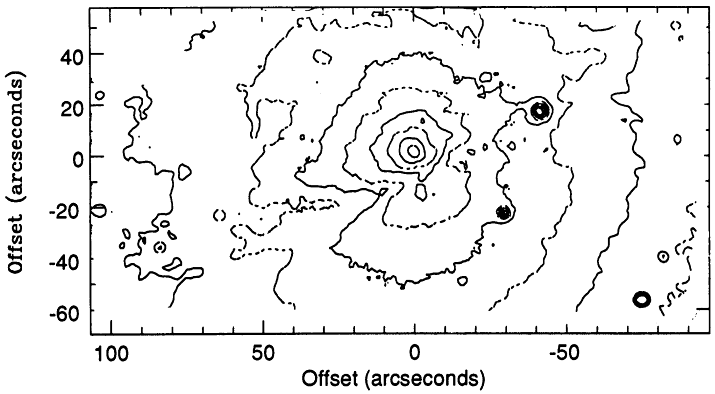

FIG. 8*a*

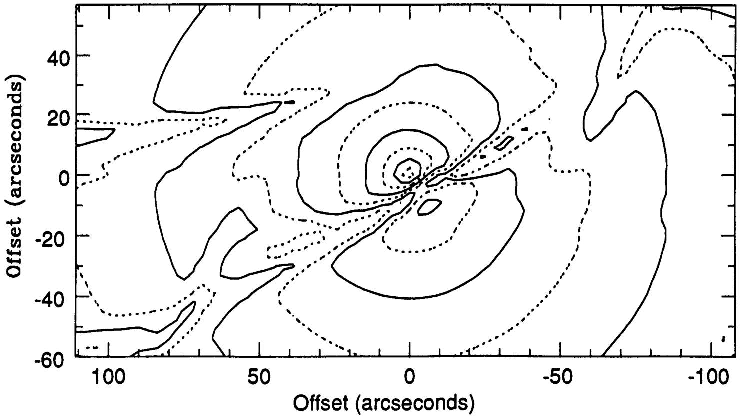

FIG. 7*b*

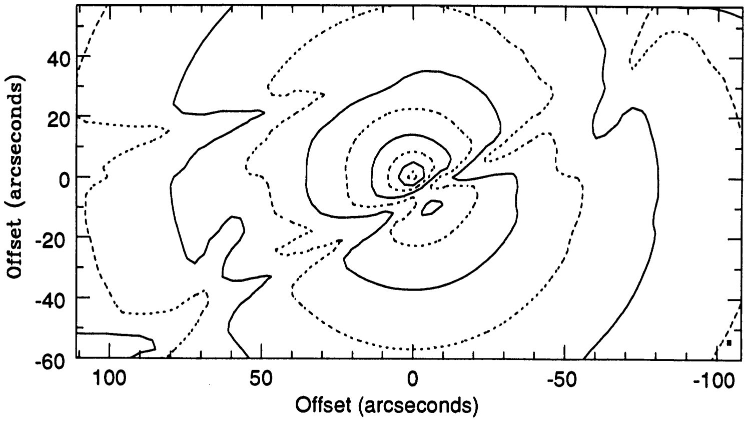

FIG. 8*b*

FIG. 7.—(*a*) *J* mosaic. The contour interval is 0.5 mag per square arcsecond with the lowest contour at the nucleus at 14.0. Brighter contours for the star 40″ to the west of the nucleus are not shown. Solid contours are at integer levels and dotted contours are at half integer levels. For $r > 40''$ from the nucleus, the data has been smoothed with a Gaussian with FWHM of 2″. Offsets are from the position from the nucleus at *K*. North is up, and east is to the left. (*b*) *J* model at same contour levels. Parameters for this model are given in Table 1. See text for further details.

FIG. 8.—(*a*) *H* mosaic. The contour interval is 0.5 mag per square arcsecond with the lowest contour at the nucleus at 12.5. Brighter contours for the star 40″ to the west of the nucleus are not shown. Solid contours are at integer levels, and dotted contours are at half integer levels. For $r > 40''$ from the nucleus, the data has been smoothed with a Gaussian with FWHM of 2″. Offsets are from the position from the nucleus at *K*. (*b*) H model at same contour levels.

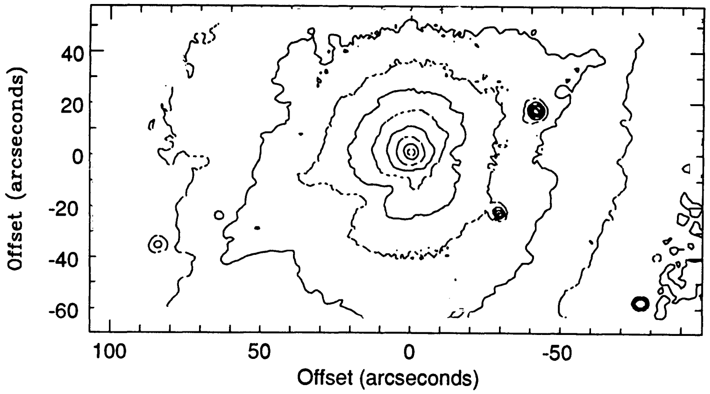

FIG. 9*a*

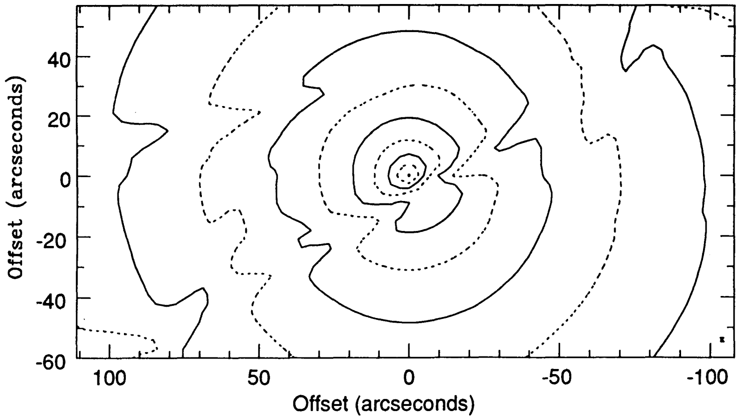

FIG. 9*b*

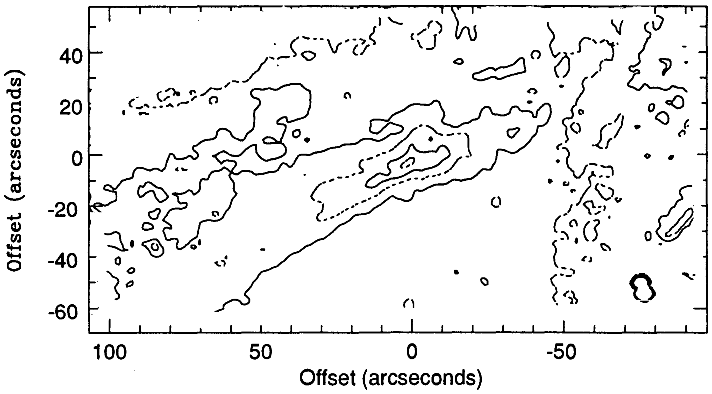

FIG. 10*a*

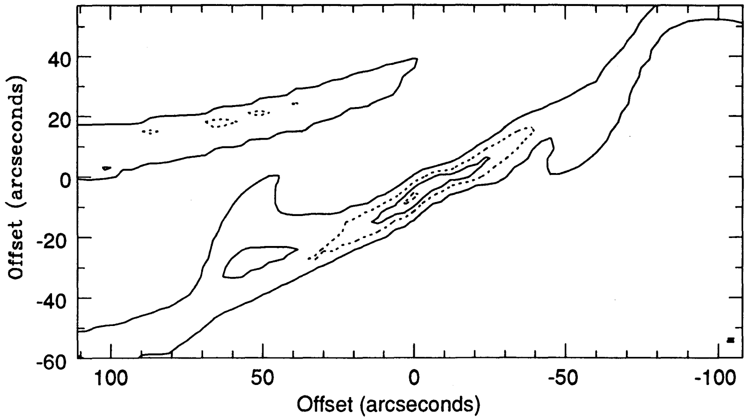

FIG. 10*b*

FIG. 9.—(*a*) *K* mosaic. The contour interval is 0.5 mag per square arcsecond with the lowest contour at the nucleus at 11.5. Solid contours are at integer levels, and dotted contours are at half integer levels. For $r > 40''$ from the nucleus, the data has been smoothed with a Gaussian with FWHM of 2''. Offsets are from the position from the nucleus at *K*. (*b*) *K* model at same contour levels.

FIG. 10.—(*a*) $J-H$ mosaic The contour interval is 0.25 mag per square arcsecond with the highest contour at 1.75. Solid contours are at multiples of 0.5, and dotted contours are at levels in between the solid contours. The data has been smoothed with a Gaussian with FWHM of 2''. Offsets are from the position from the nucleus at *K*. (*b*) $J-H$ model at same contour levels.

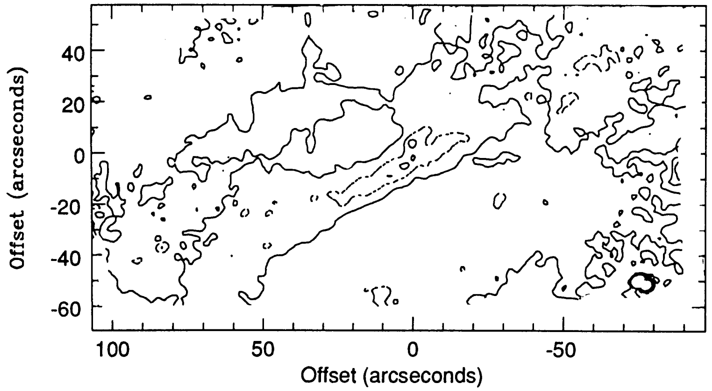

FIG. 11*a*

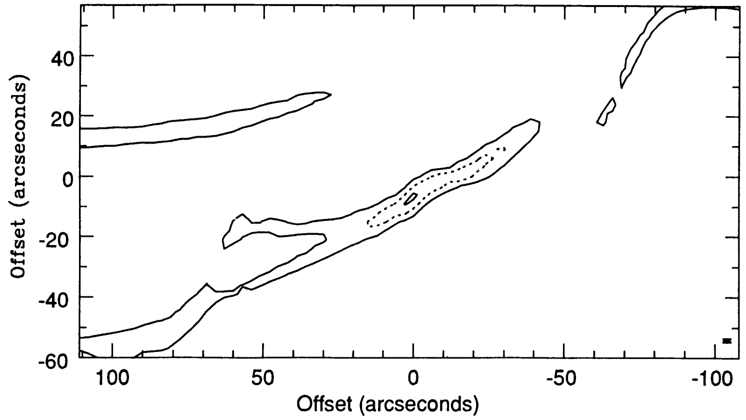

FIG. 11*b*

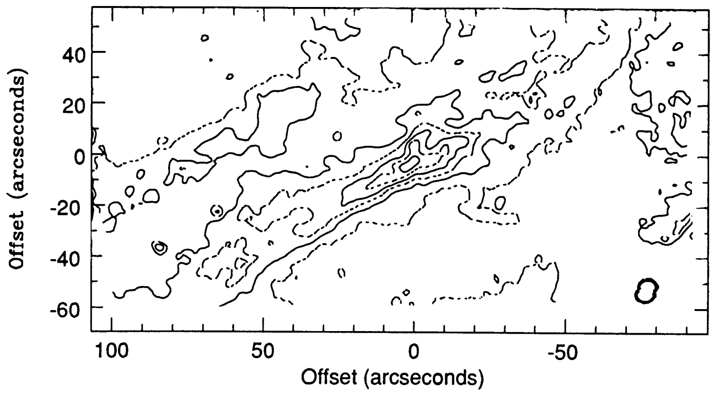

FIG. 12*a*

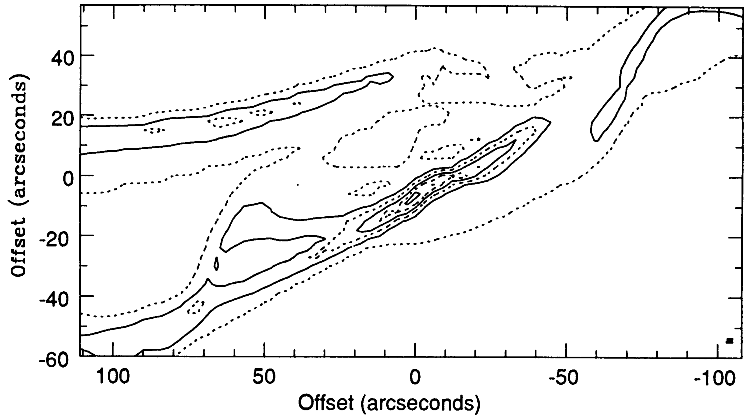

FIG. 12*b*

FIG. 11.—(*a*) $H-K$ mosaic. The contour interval is 0.2 mag per square arcsecond with the highest contour at 0.65. The spacing between the solid contours is 0.4 beginning at 0.45, and dotted contours are at levels in between the solid contours. The data has been smoothed with a Gaussian with FWHM of 2″. Offsets are from the position from the nucleus at K. (*b*) $H-K$ model at same contour levels.

FIG. 12.—(*a*) $J-K$ mosaic. The contour interval is 0.25 mag per square arcsecond with the highest contour at 2.5. Solid contours are at multiples of 0.5, and dotted contours are at levels in between the solid contours. The data has been smoothed with a Gaussian with FWHM of 2″. Offsets are from the position from the nucleus at *K*. (*b*) $J-K$ model at same contour levels.

Because of the poor resolution of our mosaics, we cannot determine if the disk is thinner than 3″ in the inner region. We note that models with $h = 2''$ at a resolution of 2″ have quite a bit more structure than is predicted in the 3″ resolution models.

4.1. *Disk Emission*

Our model does not show extensions in the higher magnitude K isophotes that are observed in the data along the disk 30″–50″ to the southeast and northwest of the nucleus. It is possible that these extensions, seen only in K, are due to emission from the warped disk. Due to the large scatter of the pixels in our color-color plot (Fig. 5), we cannot determine if the pixels in this region of the disk have different colors than expected from a purely absorptive model for the disk. However, since the purely absorptive model for the disk reproduces the colors and morphology of the rest of the data remarkably well, it is likely that these extensions in *K* are due to some emission from the disk,. We estimate that ∼17 mag per square arcseconds emission in K from the disk is necessary in order to account for the observed elongation of the isophotes in these features. We consider three possible emission sources: free-free and bound-free emission from H II regions in the disk, emission from bright giants and supergiants from the young stellar population in the disk, and emission from small hot grains of dust.

From an estimate of the maximum observed surface brightness in Hα of an H II region, we may estimate an upper limit for the maximum possible brightness expected from free-free and bound-free emission in the *K* band. J. Bland-Hawthorn (private communication) estimates that the surface brightness in Hα is at most 4×10^{-14} ergs cm^{-2} s^{-1} arcsec^{-2} per individual H II region. Phillips (1981) has observed that the H II regions in Cen A are primarily low-ionization regions with excitation temperature $T_e \sim 6500$ K, and emissivity ratio $\gamma_{\mathrm{H}\alpha}/\gamma_{\mathrm{H}\beta} \sim 3$. Using an estimate of $\gamma_K/\gamma_{\mathrm{H}\beta} \sim 2 \times 10^{14}$ Hz for these low-excitation temperatures, (Joy & Lester 1988), and multiplying these factors together, we find that the surface brightness in *K* must be less than 7 μJy arcsec^{-2} or greater than 20 mag per square arcsecond. Since the highest contour in our mosaic is at 16 mag per square arcsecond, even if the Hα flux were reddened by a few magnitudes, it is unlikely that we would detect emission from H II regions. We note that a Brγ observation in the disk would make this limit more convincing.

From a measurement of the star formation rate in the disk, we may estimate the maximum expected luminosity from the stellar component of the disk (as in Telesco & Gatley 1984). Marson et al. (1988) from the far-infrared emission from the disk estimate that the star formation rate is $\dot{M} = 1.6 \times 10^{-5}$ $M_\odot$ yr^{-1} arcsec^{-2} in the central region of the disk. Using this, the Salpeter initial mass function, and an estimate of the post–main-sequence lifetime as a function of stellar mass, $t_{\mathrm{pms}} = 1.7 \times 10^9 (m/M_\odot)^{-2.7}$ yr (Renzini 1981), we find that the number of post–main-sequence stars with mass greater than 4 $M_\odot$ (the main-sequence cutoff mass after 10^8 yr) expected is ∼10 per square arcsecond. If these stars are giants with absolute magnitude in *K* of −6, with a distance modulus of 27 to Cen A, we find that the maximum surface brightness from these stars in *K* would be ∼18 mag per square arcsecond which would be undetectable in our *K* mosaic. Similarly we estimate the number of post–main-sequence stars with mass larger than 10 $M_\odot$ to be 0.1 per square arcsecond. If these were all red supergiants of luminosity 10^6 $L_\odot$ and effective temperatures of ∼3000 K then the maximum surface brightness from these stars in *K* would be ∼18 mag per square arcsecond which would also be undetectable in our mosaic. We note that luminosity from the main sequence is also negligible, assuming that there was 10^8 yr of star formation at the star formation rate given above. If the star formation rate were higher in the recent past than is now observed, it is possible that giants and supergiants could account for the excess emission. Older stars should not be present in the disk since the time since the merger is of order 10^8 yr, and stars captured from a merging galaxy cannot settle onto a disk. We find that it is unlikely that any observed emission from the disk in *K* is due to emission from giants and supergiants in the disk.

Sellgren et al. (1984) in their observations of reflection nebulae note that under special physical conditions, the amount of UV radiation is sufficient to produce observable near-infrared emission from thermally fluctuating small dust grains, yet insufficient to create an H II region. It is possible that Cen A could satisfy these conditions since the observed H II regions are mostly low-ionization regions, yet it is evident from the far-infrared flux (Marston et al. 1988) that there is a significant amount of UV emission from newly forming stars in the disk. Existing aperture photometry in the *L* (3.5 μm) band allows us to estimate how much emission is due to small hot dust grains. Using photometry from Becklin et al. (1971) we find that the difference between the 33″ aperture magnitude and the 67″ magnitude gives a flux of ∼500 μJy per arcsecond in the annulus. If the flux level were a factor of 5 lower in *K* than at *L* (as it is observed in reflection nebulae Sellgren et al. 1984) we would measure a surface brightness of 17 mag per square arcsecond, which would be detectable in our mosaic. It is possible that we could be observing emission from small dust grains in *K*; however more data is needed to verify this. Usually excess brightness at *K* in star-forming galaxies is due to red giants and supergiants. It is therefore unexpected that dust emission is a more likely source for this emission in the disk of Cen A. It is surprising that the peculiar conditions in reflection nebulae could possibly be found on a galactic scale in the disk of Cen A.

4.2. *Nucleus of Cen A*

The location of the peak surface brightness at the nucleus in Cen A is a function of wavelength in the near infrared (Giles 1986). See Table 2 for nuclear offsets from Star A which has position R.A. $13^{\mathrm{h}}22^{\mathrm{m}}27^{\mathrm{s}}.72 \pm 0.03$ and Decl. $-42°45'19''.39 \pm 0.35$ (1950) (Griffin 1963). Within the listed errors, the nuclear position in *K* agrees with that reported by Giles (1986). However, our model does not predict any difference of position between the *J*, *H* and *K* peaks (even when integrated at higher resolution). We note that the displacement of the color peaks from the position of the *K* nucleus (see Figs. 10–12) is reproduced by our model. In our model the gas disk in the inner region only partially shields the nucleus (although it covers the nucleus at larger radii $r > 90''$). In order to account for changes in the position of the nucleus, there must be either a thick circumnuclear disk or extra folds of the warp near the nucleus. It is possible that the changing position of the nucleus is due to the circumnuclear disk (Israel et al. 1990) observed in absorption against the continuum source. The function we used for the dust surface density as a function of radius (eq [3.2]) is almost flat for $r < 60''$. However, the 2.5 mag high color peak at the nucleus observed in $J-K$ color is

1993ApJ...412..550Q

TABLE 2

NUCLEAR OFFSETS FROM STAR A

FILTER	$b = 2$			$b = 5$		
	Δ R.A.	Δ Decl.	Uncertainty	Δ R.A.	Δ Decl.	Uncertainty
J	42″89	13″08	±0″3	42″61	12″68	±0″3
H	41.52	13.59	±0.2	41.72	13.67	±0.2
K	41.02	13.53	±0.2	41.22	13.48	±0.2

NOTES.—Star A is the bright star approximately 42″ west and 13″ north of the nucleus. The location of the nuclear position is the centroid in a box of width *b* in pixels. A pixel is 0″89. Offsets are in arcseconds.

apparent in our model (see Fig. 12), and is ~4″ south of the *K* nucleus (as it is observed). Therefore the observed maximum in $J-K$ color is caused by absorption through a disk of almost constant dust surface density that is close to edge-on, not by an increase in the quantity of dust near the nucleus. The dust surface density must increase sharply at small radii ($r < 5''$) where the circumnuclear disk is located, in order to account for the peak offsets yet not effect the colors and morphology observed outside this radius.

As have Joy et al. 1991, we observe elongation (on a scale of 3″–10″) of the nucleus along the direction of the X-ray jet in the *J* and *H* mosaics. This elongation was interpreted by Joy et al. (1991) as evidence for an infrared jet. Since our model does not predict any such elongation, it is probable that excess emission along the direction of the jet is necessary in order to account for this elongation.

4.3. *X-Ray Absorption*

In this subsection we use our best-fit model for the geometry and distribution of the dust and gas to create a transmission map for X-rays which we can then compare to existing X-ray maps of Cen A. By integrating from the plane perpendicular to the line of sight containing the nucleus of Cen A out toward us we estimate an opacity $A(J)$ for every location on the sky. We expect most of the X-ray emission to be coming either from the nucleus, or from a cylinder along the direction of the jet that is lying in a plane that is close to perpendicular to the line of sight. Using $A(J)/N_{\rm H} = 1.5 \times 10^{-22}$ mag cm^2 H atom^{-1} (Mathis 1990), we may estimate the column density $N_{\rm H}$ of hydrogen atoms. A rough fit to the column density at which $\tau = 1$ (Gursky 1973) (assuming solar abundances) is

$$\log_{10}(N_{\rm H}) = 2.7 \log_{10}(E/{\rm eV}) = 13.7 , \quad (4.1)$$

where E is the energy in electronvolts and $N_{\rm H}$ is the column density of hydrogen atoms in units of H atoms cm^{-2}. Thus we may estimate at each position on the sky the energy at which the gas would become optically thick to X-rays. The result of this integration of our model is displayed as a contour plot in Figure 13.

As is predicted by our model, diffuse soft X-ray emission (<2 keV) from *EXOSAT* is observed to the north and south on either side of the disk (Morini, Anselmo, & Molteni 1989). At higher resolution with *Einstein*'s HRI (Feigelson et al. 1981) in the 0.5–4.5 keV band, a jet is observed that is one sided (Feigelson et al. 1981). The jet is observed above and below the ridge of opacity caused by the fold in the disk that runs east-west and is located ~30″ north of the nucleus. This emission along the jet must be primarily soft X-rays because it is absorbed by this fold in the disk which is not opaque to hard X-rays. Because of the high inclination of the gas disk, it is not possible to block soft X-rays over a large area on the sky. The fact that a soft X-ray jet is only observed on one side of the nucleus is not explained by our model.

At the position of maximum infrared opacity we estimate $N_{\rm H} = 2 \times 10^{22}$ cm^{-2} which is lower than the measurement at the position of the nucleus of Morini et al. (1989) of $N_{\rm H} = 1.5 \times 10^{23}$ cm^{-2}. We note that the position of maximum infrared opacity is ≈4″ to the south of the position of the K nucleus in our model. We inferred in the previous subsection that there is probably a circumnuclear disk that is not included in our

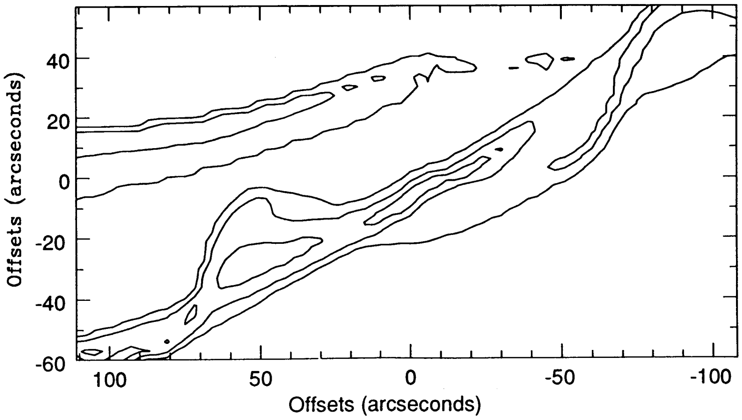

FIG. 13.—Contour map of the energy of X-rays at which $\tau = 1$ from our model. Contours are at 400, 800, and 1200 eV. See § 4.4 for details.

model which should contribute to the opacity in front of the nucleus. This may partially explain why our estimate is so low. We note that some of the X-ray opacity near the nucleus comes from a fold in the disk that is lying almost on top of the nucleus. If Cen A were at a different orientation with respect to us, it is likely that the opacity near the nucleus would be reduced.

5. DYNAMICS OF THE MERGER

In § 3.3 we reviewed the model we successfully used to fit CO data in the inner regions of Cen A (QZPP). This model assumed that the gas has evolved from a planar system as a result of differential precession (Tubbs 1980). The model that reproduced the infrared morphology had a precession angle $\alpha(r)$ described by equation (3.4), yet large changes in inclination angle, $\omega(r)$, were necessary in order to reproduce the outer fold at $r \approx 100''$ from the nucleus. *This model is therefore inconsistent with evolution by differential precession from an initially planar system.* Since the time scale for creating the warp in Cen A is short ($\sim 10^8$ yr), it is unlikely that settling onto the principal plane of the galaxy could have caused these large changes in inclination (QZPP). In this section we will discuss the possibility that the changes in inclination of the gas resulted from the dynamics of the merger.

Malin et al. (1983) have observed there is a single stellar shell at $\sim 3'$ from the nucleus of Cen A, and ~ 20 shells in a range of $7'$–$15'$ from the nucleus. They found that it is difficult to produce such a gap between stellar shells with a single accretion event. However, Dupraz & Combes (1987) find that multiple events of stripping as the galaxy spirals in under the force of dynamical friction can account for the location of shells in the inner regions of galaxies. Simulations of galaxy mergers show that multiple systems of shells over a large range of radii may be produced (Salmon, Quinn, & Warren 1989). Huang & Stewart (1987) found in their simulations that material stripped continuously will also form a sequence of stellar shells.

Because gas clouds dissipate energy during collisions, gas evolves into a configuration in which the collision rate is a minimum, such as a ring. Gas stripped tidally from a small gas-rich spiral, while spiraling into a larger elliptical galaxy, is sheared by the differential rotation rate into rings which then precess according to equation (3.3). It is likely that the radius and orientation of these rings are determined by the angular momentum of the gas at the time of stripping. Because the underlying elliptical galaxy is not spherical, the orbit of the infalling galaxy is not constrained to lie in a plane, and so the resulting gas configuration may have large changes in inclination as function of radius. Using these simple assumptions, we can determine the geometry of the gas from an integration of the orbit of the infalling galaxy. The resulting warped gas geometry can then be compared to the geometry needed to model our infrared mosaics. We expect the actual gas dynamics during the merger to be far more complicated than what is presented here, so we intend this scenario to only be a test of our simplifying assumptions.

In § 5.1 we discuss a scenario for creating the warped configuration of gas and dust based upon the reconstruction of the merger of a small spiral with a large elliptical galaxy. Gas stripped tidally from an infalling galaxy is expected to shear out into a disk or ring in a few rotation periods (Tubbs 1980). This has since been observed in smooth particle hydrodynamic simulations (Habe & Ikeuchi 1988). The orientation and radius of the gas rings are determined by the angular momentum of the gas when it is stripped from the infalling spiral galaxy. In § 5.1 we discuss the process of infall due to dynamical friction assuming that both the spiral galaxy and the elliptical can be approximated by isothermal spheres. For the merger that resulted in Cen A, we find that the spin angular momentum of the spiral galaxy can be neglected, and that the shearing time scale for the gas to spread out into a plane after stripping is of the same order of magnitude as that proposed by Tubbs (1980). We find that when the orbit of the infalling galaxy remains on a plane and the underlying galaxy has constant ellipticity, the resulting configuration of the gas is identical to that described by the model discussed in § 3.1 where the gas was initially in a plane.

In § 5.2 we discuss a numerical integration of the orbit of the infalling galaxy, and the initial conditions used for our integration. The effects on the integration of the prolate shape of the underlying galaxy and possible high ellipticity of the orbit are explored. We find an orbit that not only reproduces the changes in inclination observed in our infrared mosaics, but also reproduces the gap in the stellar shells observed by Malin et al. (1983).

5.1. *The Scenario*

In order to model the dynamics of the infalling galaxy, we need to estimate the mass of the spiral remaining after tidal stripping during the encounter. This treatment is similar to that presented by Dupraz & Combes (1987). The mass of the spiral left after stripping is determined roughly by the radius r_s from the nucleus of the spiral at which the tidal force of the elliptical on the spiral is equal to its binding force

$$\frac{M_e(D) r_s}{D^3} = \frac{M_s(r_s)}{r_s^2}, \tag{5.1}$$

where $M_e(D)$ is the mass of the elliptical galaxy inside radius D, the distance of the spiral from the nucleus of the elliptical, and $M_s(r_s)$ is the mass of the spiral inside radius r_s (which can be thought of as a stripping radius). Since spiral galaxies commonly have a flat rotation over a wide range of radii, we may approximate the spiral galaxy as an isothermal sphere. The rotation curve (assuming constant mass to light ratio) that corresponds to the observed de Vaucoulers luminosity profile of NGC 5128 (Dufour et al. 1979) is close to flat from $r \approx 70''$ to $r \approx 15'$ (the location of outermost stellar shell (Malin et al. 1983) from which we estimate the impact parameter of the collision that resulted in the merger). Over this range of radii, the elliptical galaxy may also be approximated as an isothermal sphere. The mass inside radius r for an isothermal sphere with velocity dispersion σ, is

$$M(r) = \frac{2\sigma^2 r}{G}. \tag{5.2}$$

Approximating both galaxies as isothermal spheres we estimate r_s to be

$$r_s = \frac{\sigma_s}{\sigma_e} D \tag{5.3}$$

where σ_e and σ_s are the velocity dispersions of the elliptical and spiral, respectively. Using the two previous equations we find that $M_s(D)$, the mass of the spiral galaxy, when it is at distance D is

$$M_s(D) = \frac{2\sigma_s^2 r_s}{G} = \frac{2\sigma_s^2 D}{G}\left(\frac{\sigma_s}{\sigma_e}\right). \tag{5.4}$$

1993ApJ...412..550Q

The mass stripped from the spiral dM as it falls a distance dD is

$$\frac{dM}{dD} = \frac{2\sigma_s^2}{G}\left(\frac{\sigma_s}{\sigma_e}\right). \tag{5.5}$$

From this we can see that dM/dD is roughly constant, and that material from the spiral galaxy will be at a radius in the elliptical galaxy that is a factor of σ_e/σ_s larger than the distance that it was from the center of the spiral galaxy before stripping. Because of this we expect there to be gas quite far out in the elliptical galaxy, as is observed by Malin et al. (1983) (out to 11 kpc), and in other galaxies that are the results of mergers (e.g., NGC 4753; Steiman-Cameron et al. 1992).

The geometry of the gas will be primarily determined by the angular momentum of the gas during stripping. The resulting angular momentum per unit mass of the gas after stripping is $L_{\rm orb} + L_{\rm spin}$, where $L_{\rm orb}$ is the orbit angular momentum per unit mass of the infalling galaxy and $L_{\rm spin}$ is the spin angular momentum per unit mass of the gas at the stripping radius of the infalling spiral galaxy. The amount of molecular material in Cen A, $2 \times 10^8\ M_\odot$ (Phillips et al. 1987), is roughly one-fifth that found in our Galaxy. Assuming that both our Galaxy and the small spiral believed to have fallen into the center of Cen A, are isothermal spheres, that galactic mass scales with gas mass, and that the circular velocity of our galaxy in the outer regions is $\sim$220 km s^{-1}, we estimate the velocity dispersion of the small spiral σ_s to be $\sim$70 km s^{-1}. We have assumed that the amount of the molecular gas that has been dissociated during the merger is not significant. The velocity dispersion of Cen A has been measured to be 150 km s^{-1} (Wilkinson et al. 1986), whereas the circular rotation speed has been measured to be $\sim$300 km s^{-1} (QZPP). Wilkinson et al. (1986) demonstrate by simulating the effect of the dust lane on their observations, that the dust lane can cause the velocity dispersion to be underestimated, so it is likely that their measurement σ_e is lower than the real value. Taking $\sigma_e = v_c/(2)^{1/2}$, we infer that $\sigma_e/\sigma_s \approx 3$. We note that using the Tully-Fisher relation to estimate the mass of the small spiral galaxy would have lowered this ratio. The orbital angular momentum per unit mass of the infalling galaxy is $\sim L_{\rm orb} \approx Dv_c$. The spin angular momentum per unit mass of gas stripped from the infalling galaxy at the stripping radius r_s is approximately $L_{\rm spin} \approx (\sigma_s/\sigma_e)v_c\, r_s$. Using equation (5.3) we find that

$$L_{\rm spin}/L_{\rm orb} \approx \left(\frac{\sigma_s}{\sigma_e}\right)^2 \approx \frac{1}{9}, \tag{5.6}$$

so that for Cen A, the angular momentum and resulting geometry of the gas is primarily determined by the orbit of the infalling galaxy. As a result we neglect the spin angular momentum in our models.

It has been proposed by Tubbs (1980) (and later observed in smooth particle hydrodynamic simulations Habe & Ikeuchi 1988) that smearing of captured gas into a disk or ring should occur over a few orbital periods. After stripping we expect the gas to be in a stream of width of order r_s. The shearing time scale $t_{\rm shear}$ or the time scale for a blob of gas of width r_s at distance D from the nucleus to be sheared by differential rotation is of order

$$t_{\rm shear} \sim t_D \frac{D}{r_s} \sim t_D \frac{\sigma_e}{\sigma_s} \tag{5.7}$$

which is consistent with the time scale proposed by Tubbs (1980).

A generalization of the model discussed in § 3.3 can be made by assuming that the length of time a ring at radius r has precessed depends upon the time since the gas in the ring was stripped from the infalling galaxy, and that the radius and initial angles of the ring depend upon the angular momentum of the gas at stripping. This is equivalent to assuming that Δt, and α_0 of equation (3.4) are functions of r. In this case equation (3.4) becomes

$$\alpha(r) = \alpha_0(r) + \epsilon_p \Omega \Delta t(r) \tag{5.8}$$

for $\Delta t(r) = \Delta t_0 + t_{\rm sink}(r)$, where Δt_0 is the time since the infalling galaxy reached the nucleus, $t_{\rm sink}(r)$ is the time the spiral took to spiral into radius r, and $\alpha_0(r)$ is determined from the angular momentum vector of the gas when it was stripped.

In order to estimate $t_{\rm sink}(r)$ we must integrate the equations of motion of the spiral galaxy as it is spiraling into the elliptical under the force of dynamical friction. Since the frictional force is tangential, the spiral galaxy loses angular momentum. If the orbit is close to circular we may estimate that

$$D\frac{dD}{dt} = -0.428\,\frac{GM_s(D)}{v_c}\ln\Lambda \tag{5.9}$$

(Binney & Tremaine 1987), where for elliptical galaxies, the Coulomb logarithm $\ln\Lambda$, is typically of order 21. Using our previous estimate for $M_s(D)$ we obtain

$$\frac{dD}{dt} = -0.428\ln\Lambda\left(\frac{\sigma_s}{\sigma_e}\right)^3 v_c \tag{5.10}$$

for the infall rate which is approximately constant. The resulting orbit for the infalling spiral galaxy is a logarithmic spiral. The time for the spiral to fall into the nucleus from radius D, $t_{\rm sink}(D)$, is

$$t_{\rm sink}(D) = \frac{D}{dD/dt} = t_D\left(\frac{\sigma_e}{\sigma_s}\right)^3 \frac{1}{0.428\ln\Lambda} \tag{5.11}$$

where $t_D = 1/\Omega$ is the dynamical time scale at radius D. Numerical simulations of dynamical infall time scales in a self-consistent potential agree with this expression to within an order of magnitude (Sterl Phinney, private communication).

Using the previous expression for $t_{\rm sink}$ and equation (5.8), we find that

$$\alpha(r) = \alpha_0(r) + \epsilon_p \Omega \Delta t_0 + \frac{1}{0.428\ln\Lambda}\left(\frac{\sigma_e}{\sigma_s}\right)^3 \epsilon_p\,. \tag{5.12}$$

If the background galaxy has constant ellipticity ϵ_p, and if $\omega(r)$ and $\alpha_0(r)$ are constant, then the third term in the previous equation is a constant, and the resulting models are identical to those discussed in § 3.3, where we assumed that the gas was initially on a plane. This would be the result of a planar orbit where the orientation of angular momentum vector of the infalling galaxy is roughly conserved. At time Δt_0, when the infalling galaxy reaches the nucleus, the gas stripped from the galaxy would be lying in a plane. This may partially explain why Tubbs's (1980) model in which the initial configuration for the gas is a plane has been so successful. Over a limited range of radii where the orbit of the infalling galaxy remains on a plane, we expect Tubb's model to give a good approximation for $\alpha(r)$. This may explain why we previously found such a good fit to our CO data (see QZPP) using this model and why it has been so successful in modeling the morphology of other galaxies (e.g., the remarkably twisted disk of Steiman-Cameron et

1993ApJ...412..550Q

al. 1992). We note that small variations in ϵ_p with radius can produce large variations in $\alpha(r)$. In the central regions ($r < 70''$ where the rotation curve drops), the potential of the elliptical galaxy cannot be approximated as an isothermal sphere, and the previous equation is no longer valid.

5.2. *Numerical Integration of Infalling Orbit*

In a nonspherical galaxy it is necessary to numerically integrate the equation of motion in order to determine the orbit of an infalling galaxy. In this section we give the equation of motion and describe our choice of initial conditions for the integration.

Using a fourth-order Runge-Kutta numerical integrator integrator with adaptive step size, we integrated the equation of motion of the infalling galaxy that spirals into the elliptical galaxy under the force of dynamical friction. The potential used for the elliptical galaxy is that of a logarithmic prolate, $\varphi(\boldsymbol{x}) = v_c^2 \ln s$, where $\boldsymbol{x} = (x, y, z)$ and $s = (x^2 + y^2 + z^2/q^2)^{1/2}$. For a prolate potential $q > 1$ and $\epsilon_p = 1 - 1/q > 0$. The equation of motion for the spiral galaxy is

$$\frac{d\boldsymbol{v}}{dt} = -\nabla\varphi(\boldsymbol{x}) - \eta 4\pi(\ln \Lambda)G^2\rho(\boldsymbol{x})M_s(\boldsymbol{x}) \times \left[\operatorname{erf}(X) - \frac{2X}{\sqrt{\pi}}e^{-X^2}\right]\frac{\boldsymbol{v}}{|\boldsymbol{v}|^3}, \tag{5.13}$$

where $\boldsymbol{v}$ is the velocity of the spiral, $\boldsymbol{x}$ is its position in the elliptical, $X = |\boldsymbol{v}|/v_c$, $\rho(\boldsymbol{x}) = \nabla^2\varphi(\boldsymbol{x})/4\pi G$ is the density of the background elliptical galaxy at $\boldsymbol{x}$, and $M_s(\boldsymbol{x})$, the mass of the spiral when it is at $\boldsymbol{x}$, approximated by

$$M_s(\boldsymbol{x}) = \left(\frac{\sigma_s}{\sigma_e}\right)\frac{2\sigma_s^2 s}{G}. \tag{5.14}$$

The dynamical friction term in equation (5.13) is derived from the Chandrasekhar dynamical friction formula assuming that the velocity distribution of the background galaxy is both isotropic and Gaussian (Binney & Tremaine 1987, eq. [7–18]); η represents a correction factor to the size of the dynamical friction term in order to compensate for the fact that the velocity dispersion of a self-consistent model for the galaxy would be smaller than that of an isothermal sphere. We chose $\eta = 2.0$ since the velocity dispersion of the Hernquist model (Hernquist 1990) for the range of radii of our integration gives this factor difference in the equation of motion (eq. [5.13]). Integration of these equations of motion using a anisotropic velocity dispersion did not significantly change the shape of the resulting orbit (for $\sigma_x/\sigma_z \sim 1/q \sim 0.8$). This is not surprising because the difference in the dynamical friction force is of quadrupole order in the integral over the stellar velocity distribution (see eq. [7–14] Binney & Tremaine). If the orbit is highly elliptical, stripping will not proceed at a constant rate. When s increased, we did not allow the mass of the infalling galaxy to increase.

From the integration of the orbit of the infalling galaxy we determine the configuration of the gas stripped along the orbit. The angular momentum per unit mass of material stripped at any point on the orbit of the infalling galaxy is $\boldsymbol{L} = \boldsymbol{x} \times \boldsymbol{v}$. Material stripped will form a ring at radius r which we estimate to be at $r = |\boldsymbol{L}|/v_c$. The inclination $\omega(r)$ of the resulting gas ring is given by

$$\cos[\omega(r)] = L_z/|\boldsymbol{L}|, \tag{5.15}$$

and the angle $\alpha_0(r)$ at the time of stripping is given by

$$\cos[\alpha_0(r)] = \frac{L_x}{|\boldsymbol{L}|\sin\omega(r)}. \tag{5.16}$$

Since angular momentum of an orbit is not conserved in a nonspherical potential, the resulting inclination of gas stripped from the infalling galaxy $\omega(r)$ will not in general be constant. After stripping, the gas ring is free to precess as in our previous model with precession rate given by equation (3.3), so that the angle $\alpha(r)$ for the system at a later time is

$$\alpha(r) = \alpha_0(r) + \epsilon_p\Omega(t_{\rm sink}(r) + \Delta t_0) \tag{5.17}$$

(see analogous eq. [3.4]). We note that the integration for $r < 100''$ (near where the rotation curve begins to drop) is not accurate because Chandrasekhar's dynamical friction formula is no longer valid when the mass of the infalling object at radius r is small when compared to the mass of the surrounding galaxy inside r. Therefore we used $t_{\rm sink}(r)$ to be the time since the infalling galaxy deposited material at $r = 120''$, and we used Δt_0 to be the time since the infalling galaxy deposited material at $r = 120''$.

In order to reduce the number of possible parameters, we decided to restrict the starting point of the numerical integration to the particular family of initial conditions described below. We began our orbit at a radius from the nucleus that is of the same order as the impact parameter of the encounter which is estimated to be roughly $b = 15'$ from the nucleus. Close to circular orbits for the infalling galaxy were chosen, since Huang & Stewart (1987) found that coherent and concentric shell structures (as observed in Cen A) resulted from this type of orbit. We assume our potential was prolate with z-axis along the extended direction. Because the potential we used is rotationally symmetric, we only consider incoming trajectories with a velocity vector that lies in the x-z plane

$$\boldsymbol{v} = v_0(\sin\delta, 0, \cos\delta), \tag{5.18}$$

where δ is the angle between the velocity vector and the z axis. For a straight line trajectory, the position of closest approach, **b**, can be parameterized by b_0 and ϵ, where ϵ is the angle between b and the x-axis and $\boldsymbol{b}$ is given by

$$\boldsymbol{b} = b_0(\sin\epsilon\cos\delta, \cos\epsilon, -\sin\epsilon\sin\delta). \tag{5.19}$$

We arbitrarily began our integrations at this point $\boldsymbol{b}$ with velocity $\boldsymbol{v}$ and mass M_s given by equation (5.14). We treated b_0, v_0, δ, and ω_0 as free parameters, where the initial inclination, ω_0, of the orbit is given by $\cos\omega_0 = -\cos\epsilon\sin\delta$. We searched parameter space for orbits that displayed inclination changes similar to those needed to model our infrared data.

Figure 14 shows the results of an integration for the orbit with initial conditions and parameters summarized in Table 3. For our integration we chose $\sigma_s/\sigma_e = 1/3$ (see § 5.1 for discussion), and $q = 1/0.8$ (0.8 is the axis ratio of the optical isophotes (Dufour et al. 1979). Since the approximations that went into this integration were crude, our results are intended to be mostly illustrative rather than predictive.

Figure 14*a* shows $\omega(r)$ (solid line) from the integration and the function (dotted line) we used to generate our infrared models (Figs. 7*b*–12*b*). Large changes in inclination are present in this integration, in particular the inclination is much higher at large radii than at smaller radii. In a galaxy in which the velocity dispersion is close to isotropic, dynamical friction not only circularizes an orbit (Casertano, Phinney, & Villumsen

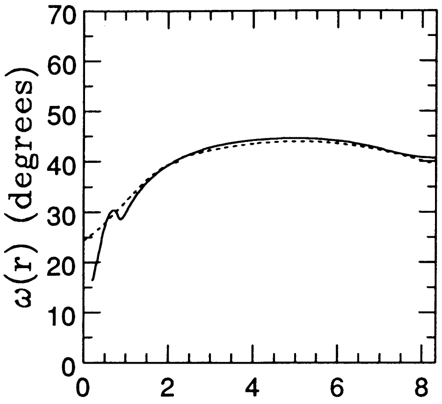

FIG. 14*a*

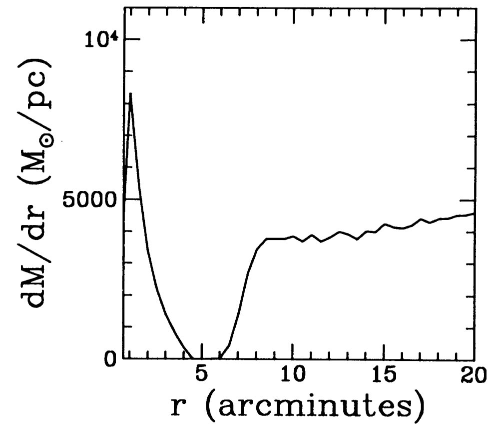

FIG. 14*b*

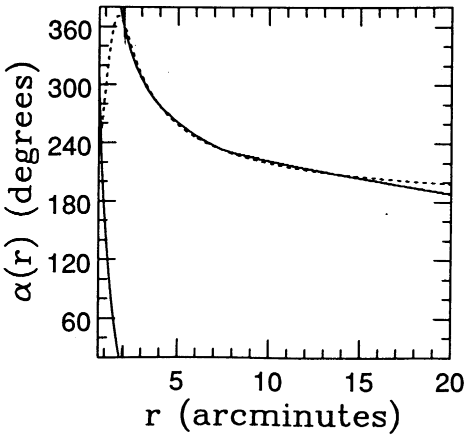

FIG. 14*c*

FIG. 14.—Gas configuration resulting from a numerical integration of an infalling orbit. Parameters of the intergration are given in Table 3. Angles are given in degrees. See § 5 for details. (*a*) The solid line is the inclination angle $\omega(r)$ resulting from the numerical integration. The dotted line is the function we used to generate the models for the mosaics (§ 3). (*b*) The mass surface density (in $M_\odot$/pc) of material stripped from the infalling galaxy as a function of radius. (*c*) The solid line is the precession angle $\alpha(r)$ at the present time resulting from the numerical integration. The dotted line is the function (equation (3.4) with parameters given in Table 1) we used to generate the models for the mosaics (§ 3).

TABLE 3

PARAMETERS FOR INTEGRATION OF ORBIT[a]

Parameter	Value
ω_0	35°
δ	65°
b_0	45′
v_0 (km s^{-1})	410
η	2
σ_s/σ_e	1/3
q	1.2
$t(r = 120'')$ (yr)[b]	6×10^7

[a] Displayed in Fig. 14. See § 5 for details.

[b] Time since the infalling galaxy reached $r = 120''$ from the nucleus.

1987), but also may cause an orbit to settle onto the principal plane of a galaxy.

Figure 14*b* shows the mass density as a function of radius of material stripped from the infalling galaxy. Material is stripped continuously at radii greater than $r = 7'$ and dM/dD is roughly constant, as we estimated in § 5.1. There is also material stripped at radii less than 3′, the location of the innermost shell (Malin et al. 1983), and where the dust lane is found. However, there is a gap in radii where no material is stripped for $r = 3'$–$7'$. This gap results from an apocenter in the infalling orbit. When the orbit of the infalling galaxy is sufficiently elliptical, there can be regions of the orbit that are far enough away from the nucleus that stripping will cease (Dupraz & Combes 1987). We note that Malin et al. (1983) had difficulty accounting for the location of this inner shell and the size of the gap separating it from the others, assuming that Cen A resulted from one accretion event. The results of our integration seem to provide a natural explanation for this gap.

Figure 14*c* displays $\alpha(r)$ at the present time (solid line) with $t(r = 120'') = 6.0 \times 10^7$ years since the infalling galaxy was at $r = 120''$. The dotted line in this figure is $\alpha(r)$ from our previous model (eq. [3.4]). A constant has been added to the result of the integration in order to match the precession angle of our previous model at $r = 120''$. The resulting precession angle $\alpha(r)$ is well fitted by a function that is proportional to the angular rotation rate Ω and so is consistent with the precession model (Tubbs 1980), (and the geometry we used to model the infrared data) but has been generated by our integration which allows the gas to precess since the time of stripping. Our integration confirms our result of § 5.1 that the precession angle can be well described by a function that is identical to the precession model in which the initial condition is a planar configuration for the gas. The primary difference between the results of the integration and our previous model (§ 3.1) consists of changes in inclination.

Material from the infalling galaxy currently at radius r has angular momentum vector given by $\alpha(r)$ (Fig. 14*c*) and $\omega(r)$ (Fig. 14*a*). At a radius $r \sim 6'$, the orientation of the angular momentum vector has $\omega = 45°$ and $\alpha \approx 240°$. Using equations (7.3) and (7.4) from (QZPP) we find this vector has a position angle on the sky of about $-20°$ which is consistent with the rotation axis of planetary nebulae at $8' < r < 20'$ observed by (Ford et al. 1989 and Hui 1990) at a position angle of about 25° and the rotation axis observed from H I in this same region (J. van Gorkom, private communication). We note that this axis of rotation is coincident with the direction of stellar rotation observed by Wilkinson et al. (1986). Our integration is also consistent with the rotation axis of the gas in the inner region ($r < 70''$) which has a position angle of $\sim 30°$. We find that our integration provides a natural explanation for the observed large change in the position angle of the rotation axis.

From our integration we estimate that the time since the spiral galaxy was at the position of the outer stellar shells at $\sim 15'$ (Malin et al. 1983) was 1.6×10^8 yr. At this radius the dynamical time $t_D \approx 4.5 \times 10^7$. This time is shorter than our estimate given in equation (5.11). Huang & Stewart (1987) found that sinking times in nonspherical potentials were significantly smaller than those in spherical ones. We note that our estimated time is not long enough to produce the number of observed stellar shells at this radius ($r \sim 15'$) assuming that these shells originated from one accretion event. However, if material is stripped at a variety of different radii (as is seen in our integration) more shells would be produced. At this time scale, the gas has not had time to shear out completely into a ring, and so the individual gas clouds stripped should not have collided with themselves. We do not expect the gas at this radius to have settled onto a planar surface. Emission from atomic hydrogen emission observed aligned with these shells (J. van Gorkom, talk given at 3d Teton Astronomy Conference 1992 July, private communication) supports our short estimate for the time scale since the merger, since we would expect the gas to be on the same orbits as stars stripped from the infalling galaxy.

6. DISCUSSION AND SUMMARY

In this paper we present new large-scale infrared mosaics in J, H, and K of the dust lane of Cen A. By integrating the light of the galaxy through an absorptive warped disk, we successfully model the morphology and colors of our data. The model we used for the geometry of the warped disk is consistent with kinematics of the CO (QZPP) and Hα (Nicholson et al. 1992) data.

Elongation along the direction of the soft X-ray jet in the isophotes at J and H is not predicted at the nucleus in our models, so we support the interpretation (Joy et al. 1991) of this elongation as evidence for an infrared jet. We do not observe a shift in the position of the nucleus (reported by Giles 1986) with respect to the K nucleus in our models at J and H. This shift could be caused by the circumnuclear disk observed by (Israel et al. 1990), which is not part of our model.

Observed extensions of the K isophotes $30''$–$50''$ from the nucleus, are not predicted in our model. A likely explanation is that they are caused by emission from the disk. We find that it us unlikely that this emission is from H II regions or from red giants and supergiants in the disk, but that this emission may be from thermally fluctuating small hot dust grains. This is unexpected since excess brightness at K in star-forming galaxies is usually due to red giants and supergiants. It is surprising that the physical conditions in the disk of Cen A could be similar to those found in reflection nebulae, but on a galactic scale. Higher quality near- and far-infrared observations of the disk of Cen A are needed to confirm this possibility.

Our model is consistent with existing X-ray observations of Cen A. In Figure 13, we show an X-ray transmission map predicted by the model, that can be compared to future higher resolution X-ray observations of Cen A. We find that some of the high X-ray opacity near the nucleus is caused by the location of a fold in the gas and dust disk near the nucleus. If the orientation of the galaxy with respect to us were slightly different, we would expect the X-ray opacity at the nucleus to be reduced. Observation of a one-sided soft X-ray jet (Feigelson et al. 1981) is not explained by our model.

We find that the model for the geometry of the warp needed to reproduce the morphology of our near-infrared mosaics has a precession angle identical to that successfully used to model the kinematics of the CO data (QZPP) for $r < 70''$, which is derived assuming that the disk has evolved as result of differential precession (Tubbs 1980). However, the disk has an inclination, with respect to the principal axes that is higher at larger radii than in the inner region, and so is inconsistent with precession from an initially planar system. Since the time scale needed to create the warp is short ($\approx 10^8$ yr) (Tubbs 1980; QZPP), it is unlikely that settling onto the principal plane of the galaxy could have occurred on this time scale.

In § 5, we propose a scenario in which gas stripped tidally from an infalling galaxy forms a ring with radius and orientation determined by the angular momentum of the infalling galaxy at the time of stripping. Afterward, the gas rings are free to precess in the potential of the underlying galaxy. Stripping at different times during the infall produces a smoothly connected system of rings, or a warped geometry for the gas. In a nonspherical potential, the orbit of the infalling galaxy is not constrained to lie on a plane, so that the resulting inclination of the gas rings with respect to the principal axes of the potential is not expected to be constant as a function of radius.

In § 5, by considering the infall under dynamical friction of a small isothermal sphere into a larger one, we find that under certain conditions (the orbit of the infalling galaxy is close to circular and is on a plane, and the underlying galaxy has constant ellipticity), the resulting gas configuration is identical to that described by the precession model in which the gas is assumed to be initially on a plane (Tubbs 1980). By numerically integrating an orbit, we find that there can be large changes in inclination of the gas as a function of radius, but that the precession angle can still be described by the precession model (Tubbs 1980). We find an orbit that not only reproduces the changes in inclination needed to reproduce the morphology of our mosaics, but also reproduces the gap in the stellar shells observed by Malin et al. (1983). This orbit also provides a natural explanation for the difference in the rotation axis observed from planetary nebulae (Ford et al. 1989; Hui 1990) and H I (J. van Gorkom, private communication) in the outer part of the galaxy, and the rotation axis of the gas in the inner region ($r < 70''$). From our orbit we find that the time since the merger (since the infalling galaxy was at $\sim 15'$ from the nucleus) is remarkably short (1.6×10^8 yr). Whie observations of H I aligned with stellar shells in this region (J. van Gorkom, private communication) suggest a short time scale, it is possible that we could have underestimated the time scale due to the crudeness of the numerical integration of our orbit.

The gas in AGNs is observed to be nonplanar and misaligned from the host galaxy in both radio Seyferts (Unger et al. 1987; Haniff, Wilson, & Ward 1988), and in radio ellipticals (Sansom et al. 1987). Our scenario suggests one mechanism for how gas can become nonplanar and misaligned within the host galaxy.

It has recently been proposed by Thomson (1992) that part of the spiral galaxy that was involved in the merger of Cen A was ejected and formed the Fourcade Figueroa shred (an apparently irregular blue galaxy a few hundred kiloparsecs from Cen A). This is a fascinating possibility. In their scenario, the core of the spiral galaxy escapes after the collision and forms a dwarf elliptical galaxy. While it is possible that material could have been ejected during the merger, it is unlikely that the core of the spiral galaxy did not merge into the large elliptical galaxy.

It has been suggested that warped disks could be used to prove the three-dimensional mass distribution of galaxies (Steiman-Cameron et al. 1990). We find that in a galaxy in which the warped disk resulted from a merger, such a study may be complicated by the dependence on the final configuration of the disk on the details of the merger. Attempts to probe the potential of host galaxies using stellar shells will be subject to the same complications.

The approximations that went into our numerical integration of the orbit of the infalling galaxy were crude. We hope that the process of the merger of Cen A will be modeled numerically with an *N*-body code which includes gas particles. Such an experiment could verify our scenario, as well as investigate what happens when the infalling galaxy reaches the nuclear region of the underlying galaxy. Improvements in *N*-body numerical methods and hydrodynamical codes in the past decade, along with the present detailed knowledge of the gas and stars in Cen A might make reexamination of these issues exciting.

We gratefully thank D. DePoy and the CTIO staff for help with the observations. T. de Zeeuw provided the original motivation for this work. This paper could not have been written without his help. I thank the Submillimeter and Infrared Research Groups at Caltech for their support and help. I also acknowledge useful discussions and correspondence with T. de Zeeuw, E. S. Phinney, J. Bland-Hawthorn, J. van Gorkom, S. Sridhar, and B. Ratra. This research was supported in part by NSF grant AST 90-15755, and NASA grants NAGW-2144 and NAGW-2142.

REFERENCES

Baade, W., & Minkowski, R. 1954, ApJ, 119, 215
Becklin, E. E., Frogel, J. A., Kleinmann, D. E., Neugebauer, G., Ney, E. P., & Strecker, D. W. 1971, ApJ, 170, L15
Binney, J., & Tremaine, S. 1987, Galactic Dynamics (Princeton Univ. Press)
Bland, J., Taylor, K., & Atherton, P. D. 1987, MNRAS, 228, 595 (BTA)
Casertano, S., Phinney, E. S., & Villumsen, J. V. 1987, in IAU Symp. 127, Structure and Dynamics of Elliptical Galaxies, ed. P. T. de Zeeuw (Dordrecht: Reidel), 474
Dufour, R. J., van den Bergh, S., Harvel, C. A., Martins, D. H., Schiffer, F. H., Talbot, D. L., & Wells, D. C. 1979, AJ, 84, 284
Dupraz, C., & Combes, F. 1987, A&A, 185, L1
Eckart, A., Cameron, M., Rothermel, H., Wild, W., Zinnecker, H., Rydbeck, G., Olberg, M., & Wiklind, T. 1990, ApJ, 363, 451
Elias, J. H., Frogel, J. A., Matthews, K., & Neugebauer, G. 1982, AJ, 87, 1031
Feigelson, E. D., Schreier, E. J., Delvaille, J. P., Giacconi, R., Grindlay, J. E., & Lightman, A. P. 1981, ApJ, 251, 31
Ford, H. C., Ciardullo, R., Jacoby, G. H., & Hui, X. 1989, in IAU Symp. 131, Planetary Nebulae, ed. S. Torres-Peimbert (Dordrecht: Reidel), 335
Frogel, J. A., Persson, S. E., Aaronson, M., & Mathews, K. 1978, ApJ, 220, 75
Giles, A. B. 1986, MNRAS, 218, 615
Griffin, R. F. 1963, AJ, 68, 421
Gurskey, H. 1973, in Black Holes, ed. C. De Witt & B. S. De Witt (New York: Gordon & Breach), 302
Habe, A., & Ikeuchi, S. 1988, ApJ, 326, 84
Haniff, C. A., Wilson, A. S., & Ward, M. J. 1988, ApJ, 334, 104
Heckman, T. M., Carty, T. J., & Bothum, G. D. 1985, ApJ, 288, 122
Heckman, T. M., Smith, E. P., Baum, S. A., van Breugel, W. J. M., Miley, G. K., Illingworth, G., Bothum, G. D., & Balick, B. 1986, ApJ, 311, 526
Hernquist, L. 1990, ApJ, 356, 359
Hernquist, L., & Quinn, P. J. 1988, ApJ, 331, 682
———. 1989, ApJ, 342, 1
Huang, S.-N., & Stewart, P. 1987, A&A, 174, 13
Hui, X. 1990, talk presented at Aspen Workshop on Structure and Dynamics of Galaxies
Israel, F. P., van Dishoeck, E. F., Baas, F., Koorneef, J., Black, J. H., & de Graauw, Th. 1990, A&A, 227, 342
Joy, M., Harvey, P. M., Tollestrup, E. V., Sellgren, K., McGregor, P. J., & Hyland, A. R. 1991, ApJ, 366, 82
Joy, M., & Lester, D. F. 1988, ApJ, 331, 145
Joy, M., Lester, D. F., Harvey, P. M., & Ellis, H. B. 1988, ApJ, 326, 662
Malin, D. F., Quinn, P. J., & Graham, J. A. 1983, ApJ, 272, L5
Marston, A. P., & Dickens, R. J. 1988, A&A, 193, 27
Mathis, J. S. 1990, ARA&A, 28, 37
Morini, M., Anselmo, F., & Molteni, D. 1989, ApJ, 347, 750
Nicholson, R. A., Bland-Hawthorne, J., & Taylor, K. 1992, ApJ, 387, 503
Phillips, M. M. 1981, MNRAS, 197, 659
Phillips, T. G., Ellison, B. N., Keene, J. B., Leighton, R. B., Howard, R. J., Masson, C. R., Sanders, D. B., Veidt, B., & Young, K. 1987, ApJ, 322, L73
Quillen, A. C., de Zeeuw, P. T., Phinney, E. S., & Phillips, T. G. 1992, ApJ, 391, 121 (QZPP)
Renzini, A. 1981, Ann. Phys., 6, 87
Salmon, J. K., Quinn, P. J., & Warren, M. 1989 preprint
Sansom, A. E., Danziger, I. J., Ekers, R. D., Fosbury, R. A. E., Goss, W. M., Monk, A. S., Shaver, P. A., Sparks, W. B., & Wall, J. V. 1987, MNRAS, 229, 15
Sellgren, K. 1984, ApJ, 277, 623
Sparke, L. S. 1986, MNRAS, 219, 657
Steiman-Cameron, T. Y., & Durisen, R. H. 1988, ApJ, 325, 26
Steiman-Cameron, T. Y., Kormendy, J., & Durisen, R. H. 1992, AJ, 104, 1339
Telesco, C. M., & Gatley, I. 1984, ApJ, 284, 557
Thomson, R. C. 1992, MNRAS, 257, 689
Tonry, J. L., & Schechter, P. L. 1990, AJ, 100, 1794
Tubbs, A. D. 1980, ApJ, 241, 969
Turner, P. C., Forrest, W. J., Pipher, J. L., & Shure, M. A. 1992, ApJ, 393, 648
Unger, S. W., Pedlar, A., Axon, D. J., Whittle, M., Meurs, E. J. A., & Ward, M. J. 1987, MNRAS, 228, 671
van Albada, T. S., Kotanyi, C. G., & Schwarzschild, M. 1982, MNRAS, 198, 303
van Gorkom, J. H., van der Hulst, J. M., Haschick, A. D., & Tubbs, A. D. 1990, AJ, 99, 1781
Wilkinson, A., Sharples, R. M., Fosbury, R. A. E., & Wallace, P. T. 1986, MNRAS, 218, 297